A fast computational model for the electrophysiology of the whole human heart

Giulio Del Corso[a], Roberto Verzicco[a,b,c], Francesco Viola[a,*]

[a]*GSSI (Gran Sasso Science Institute), L'Aquila, Italy*
[b]*POF Group, University of Twente, The Netherlands*
[c]*Roma Tor Vergata, Roma, Italy*

Abstract

In this study we present a novel computational model for unprecedented simulations of the whole cardiac electrophysiology. According to the heterogeneous electrophysiologic properties of the heart, the whole cardiac geometry is decomposed into a set of coupled conductive media having different topology and electrical conductivities: (i) a network of slender bundles comprising a fast conduction atrial network, the AV–node and the ventricular bundles; (ii) the Purkinje network; and (iii) the atrial and ventricular myocardium. The propagation of the action potential in these conductive media is governed by the bidomain/monodomain equations, which are discretized in space using an in–house finite volume method and coupled to three different cell models, the Courtemanche model [1] for the atrial myocytes, the Stewart model [2] for the Purkinje Network and the ten Tusscher–Panfilov model [3] for the ventricular myocytes. The developed numerical model correctly reproduces the cardiac electrophysiology of the whole human heart in healthy and pathologic conditions and it can be tailored to study and optimize resynchronization therapies or invasive surgical procedures. Importantly, the whole solver is GPU–accelerated using CUDA Fortran providing an unprecedented speedup, thus opening the way for systematic parametric studies and uncertainty quantification analyses.

Keywords: electrophysiology, bidomain equations, heart modelling, GPU

---

*Corresponding author: **francesco.viola@gssi.it**

computing.

1. Introduction

Owing to the development of accurate mathematical models capable of virtually replicating biological systems and to the growing availability of computational resources to solve them, medical research is increasingly integrated with computational engineering [4]. In particular, the correct modelling of the heart functioning in healthy and pathologic conditions – such in the case of *ischemic* events (reduced blood supply to a portion of the myocardium leading to dysfunction and, possibly, to the necrosis of the tissue) or of *bundle branch block* (delay or blockage along the heart electrical pathway) – entails reproducing the highly cooperative and interconnected dynamics of the heart, including its complex electrical activation.

The latter involves many embedded conductive structures with different biological properties so as to rapidly propagate the electrical activation of atria and ventricles in order to achieve an efficient muscular contraction propelling the blood into the circulatory system. As shown in Figure 1 a), the cardiac electrical depolarization, corresponding to a rise in the electrical potential across the cellular membrane owing to the transmembrane flux of ions, is initiated close to the entrance of the superior vena cava at the sinoatrial node (SA–node). Within the SA–node, some specialized pacemaker cells spontaneously produce a periodic electrical impulse, the *action potential*, which propagates across the right atrium through three high speed conductivity bundles – namely the Thorel's pathway/posterior internodal tract, the Wenckebach's middle internodal tract and the anterior internodal tract – that wrap the right atrial chamber to assure a uniform activation. A branch bifurcating from the latter bundle then penetrates into the internal muscle of the left atrium (Bachmann's bundle), thus initiating the depolarization also of this chamber. Since the propagation speed of the action potential within the fast internodal bundles is of about 1–2 m/s (significantly larger than the one observed in the atrial muscle of about 0.3–0.5 m/s

2

[5, 6, 7]), after 30 ms the depolarization front reaches the atrioventricular node (AV–node) which is the electrical gate connecting the atrial with the ventricular electrophysiology system, see Figure 1(b). In the AV–node, specialized cells slow down the propagation of the transmembrane potential by about 100 ms in order to allow both atria to contract before the activation wave reaches the ventricles; this avoids the simultaneous contraction of the whole organ which would produce inefficient filling/emptying of the four chambers and impaired pumping [8]. Once beyond the AV–node, the signal propagates through the His bundle, which forks into the right and left bundle branch that, in turn, progressively divide into a plethora of thin, tightly woven specialized cells named the Purkinje network, where the propagation speed of the action potential is in the range 1.5-4 m/s, corresponding to six times the propagation speed in the ventricular muscle [5]. This fast conduction system quickly propagates the electrical signal within the ventricular myocardium (about 30 ms to reach the terminations of the Purkinje fibers) to provide an almost simultaneous contraction of the ventricular muscle. In addition, the Purkinje network also assures the timely activation of the papillary muscles, which stretch the *chordae tendineae* so to prevent the eversion of the mitral and tricuspid valve leaflets by pulling down their free margins during early systole [9]. Although the precise morphology and orientation of the Purkinje network can not be measured in–vivo, a significant variability among individuals is known to exist [10], also depending on the positions of the papillary muscles which also varies among the population [11]. Furthermore, its smaller fibers are randomly oriented in the subendocardium with a penetration length in the myocardium of about $0.5 - 100 \ \mu m$ and with an average distance among them of about 0.1 mm [12, 13]. The Purkinje fibers are electrically isolated from the myocardial muscle, except at their endpoints called *PMJs* (Purkinje Muscle Junctions), where the electrical signal can propagate from the Purkinje fibers to the ventricular myocardium with a delay ranging from to 5 to 15 ms (*orthodromic* propagation) and vice–versa from the myocardium to Purkinje with a delay of 2-3 ms (*antidromic* propagation) [14].

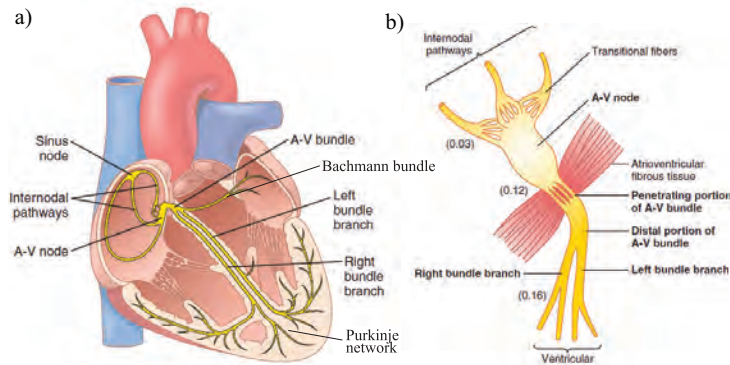Both the fast bundles and the Purkinje networks electrically activate the

3

Figure 1: Sketch of the electrophysiology system of the heart [5]. a) Fast conduction networks of bundles and Purkinje. b) Detail of the AV bundle with the corresponding activation times (in seconds) showing the propagation delay happening in the AV–node.

muscular myocardium in terms of action potential, which then propagates in the thick muscular myocardium at a lower speed that depends on the local fiber orientation. The myocardium is, indeed, an orthotropic medium [15] made of oriented myocytes that enable a faster transmission of electrical impulses in the fiber direction than in the orthogonal one and this tissue heterogeneity, playing a role in the atrial [16] and ventricular [17, 18] depolarization, should be accounted for in cardiac numerical models. According to the model proposed by Buckberg et al. [19] the muscular fibers have a dual-orientation, with directions ranging approximately from $+60°$ to $-60°$ across the ventricular wall [20] and this structure has been confirmed by accurate imaging analysis of mammalians heart [21]. An additional cause of inhomogeneity is that the ventricular myocytes have different electrical properties from the atrial ones, thus resulting in a different electrical conductivity (yielding a different propagation speed) and different ionic fluxes across the myocytes membrane, which entail a different contraction pattern of atrial and ventricular chambers.

In the last decades few mathematical models for solving the cardiac electrophysiology have been proposed. The eikonal approach solves directly the electrical depolarization of the cardiac tissue by taking as input the propagation speed within the media [22], whereas the interconnected cable methods

4

solve the propagation of an electrical stimulus thorough a connected network of discrete cables representing the myocardium [23, 24]. These methodologies have a limited computational cost and have been used to model the cardiac tissue including the macroscopic effects of structural heterogeneity on impulse propagation [25] and to incorporate more complex conduction structures, such as cardiomyocytic fibers orientation and the His–Purkinje activation network [26]. On the other hand, leveraging on the continuum hypothesis the cardiac tissue can be modeled as an intracellular and an extracellular overlapping conductive media separated by the cell membrane. The resulting bidomain model [27, 28] thus consists of the coupling between a system of reaction–diffusion partial differential equations (PDEs, governing the potential propagation in the media) and a set of ordinary differential equations (ODEs) for the cellular ionic model describing the current flow through ion channels. The bidomain model is the state–of–the–art mathematical model for reproducing the cardiac electrophysiology at a continuum level [29, 30], it has been validated against several experiments on animals [31, 32] and it is currently adopted to solve the action potential propagation in healthy and pathologic conditions including ischemic events and fibrillation [33, 34, 30]. In the case the extracellular conductivity tensor is proportional to the intracellular one, the bidomain equations can be simplified into a single governing equation for the transmembrane potential, the monodomain system, which is computationally cheaper than the bidomain counterpart as the number of degrees–of–freedom (dofs of the system of PDEs) is halved [29]. Unless complex pacing patterns or fibrillation are present, the monodomain equation can be conveniently used to approximate the bidomain solution also in the case the conductivity tensors are not proportional [35] by setting the components of the monodomain conductivity tensor to half the harmonic mean of the corresponding extracellular and intracellular components [29].

The bidomain/monodomain electrophysiology model has been widely used to study different components of the cardiac electrical network such as the atrial depolarization also including pathologic atrial fibrillation [36, 16] or to model

5

the AV–node depolarization [37, 38]. The depolarization in the ventricular my-ocardium has been investigated in a series of works [17, 39, 40, 41] also including the fast conduction Purkinje network [14, 21, 42], which is needed to reproduce a realistic ventricular depolarization, especially in the presence of infarction [43] or reentry initiation of arrhythmias [44, 45, 46]. In these works, the geometry of the Purkinje network is generally obtained by applying a *growing* algorithm to a one–dimensional (1D) network of fibers, which has to be sufficiently dense in order to correctly activate the 3D myocardium [47, 48, 49].

Although some studies are very advanced in solving the bidomain/mon-odomain equations in a portion of the cardiac electrical network [50, 51, 52, 53, 54], a comprehensive computational framework, solving simultaneously the fast conduction electrophysiology networks and the four–chambers muscular my-ocardium, is still missing. Such a computational model for the whole cardiac electrophysiology would entail, indeed, the solution of a large dynamical system, thus calling for efficient code parallelization with an effective use of the com-putational resources. This work aims at building an accurate computational framework for solving the whole cardiac electrophysiology accounting for: (i) the fast conductivity structures of the atria and ventricles including the intern-odal pathways, branch bifurcations, and the AV–node; (ii) the Purkinje network immersed in the ventricular myocardium, which activates the ventricular mus-cle at the PMJs; (iii) the thick atrial and ventricular myocardium with their muscular fibers orientation yielding electrical anisotropy. These three electrical components of the system have different electrophysiology properties and are modelled using a hierarchy of interconnected geometries having different topo-logical dimension and cell models. The bidomain/monodomain equations are discretized in space using an in–house finite volume method that allows for tack-ling complex geometries, also deforming in time, and the whole model has been ported to CUDA to run on GPU architectures thus providing unprecedented speedups [55, 4]. The resulting computational model is then applied to solve the cardiac electrophysiology in healthy and pathologic conditions with the aim of assessing the model performance and validating its results.

6

The paper is organized as follows. After the introduction of the cardiac geometry used throughout the work in § 2, the governing equations and the GPU–accelerated numerical methods are detailed in § 3. The convergence analysis of the code and validations against benchmarks results from the literature are reported in § 4. In § 5 the electrophysiology activation of the whole human heart is studied in healthy and pathological conditions, including bundle branch blocks and the implant of artificial cardiac pacemakers. Conclusions and further research directions including possible uncertainty quantification analyses are outlined in § 6.

2. Computational domain: splitting the electrophysiology system
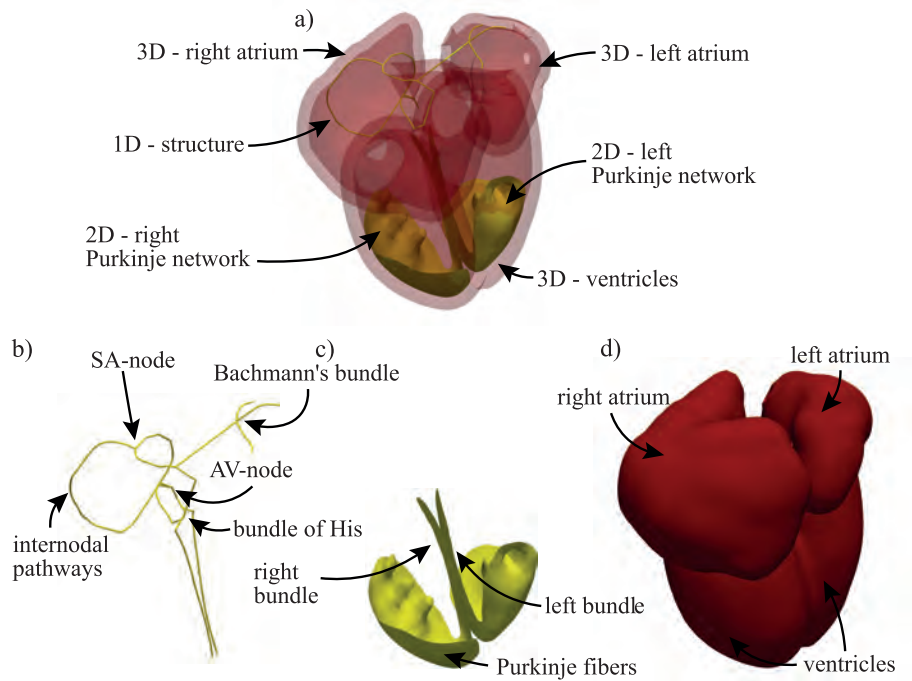

Figure 2: The a) whole cardiac electrophysiology system is split in: b) 1D network of fast conduction bundles, c) 2D Purkinje network and d) 3D myocardium.

As anticipated above, the cardiac electrophysiology system is made of a (i) fast conduction network of bundles, (ii) a Purkinje network for the ventricular

7

activation and (iii) the massive conductive myocardium contracting as the myocytes depolarize. Our computational approach is based on intrinsic connections
among different conductive media and pathways, and the complex electrophysiology system is thus split in several interconnected subdomains with different
dimensional topology (see Figure 2), namely a one–dimensional graph (1D) modelling the fast conduction bundles (panel 2 b); a two–dimensional (2D) surface
approximating the dense Purkinje network (panel 2 c); three-dimensional (3D)
media for the atrial and ventricular muscles (panel 2 d). The solution of the
complete system, shown in panel 2a, is thus obtained by the coupled solutions
of these three distinct components which are detailed in the following.

2.1. One dimensional fast conduction network of bundles
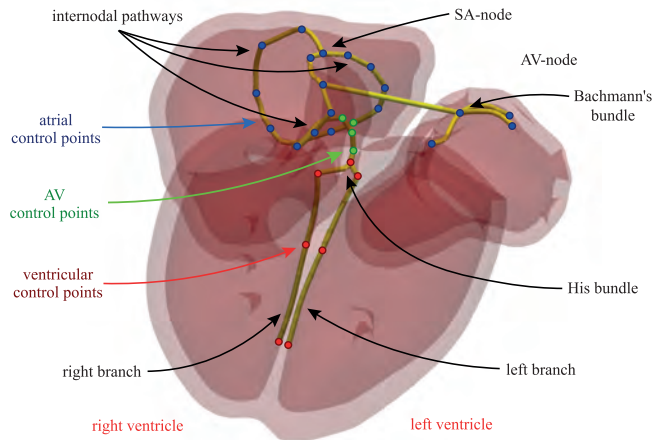

Figure 3: Fast conduction network of bundles. The circles indicate the geometrical control points of the atrial network (blue), AV–node (green) and ventricular network (red).

Owing to its slenderness, the fast conductivity structures conveying the electrical signal through the 3D myocardium has been modelled as a 1D fast conduction pathway with space–varying electrophysiology properties (see Figure 3).
The network originates from the SA–node and branches into the three internodal
pathways reaching the AV–node with one of them (the anterior internodal pathway) further branching and connecting the right atrium to the left one through

8

¹⁷⁰ the Bachmann's bundle. The terminations of the internodal pathways reach the AV–node (in two locations) connecting the atrial fast conduction network with the ventricular through the bundle of His, which then splits into two distinct branches, one immersed in the right ventricle and the other in the left one.

In order to eventually adapt the fast conduction network to different pa-¹⁷⁵ tient geometries, the entire graph is generated through a set of control points whose coordinates can be arbitrarily set so to easily reproduce a given cardiac geometry following the adaptive procedure. Specifically, 19 control points are distributed among the SA–node and the atrial bundles (indicated by blue bullets in Figure 3), 4 control points are used for the AV–node and its connection with ¹⁸⁰ the bundle of His (green bullets in Figure 3) and 7 more control points are used for the ventricular bundles (red bullets Figure 3). The pathways connecting the control points are built using a piecewise linear interpolation which are then projected over the atrial and ventricular endocardium, whereas the portions of the 1D graph lying within the ventricular septum, such as the AV–node, are im-¹⁸⁵ mersed in the 3D mesh volume. The 1D graph is then meshed uniformly with linear elements of a given grid size (much finer than the distance between two adjacent bullets). The whole procedure runs in few CPU–minutes, thus provid-ing the correct positioning of a realistic 1D conduction network within the 3D mesh, with multiples bundles branching/joining the same nodes, as shown in ¹⁹⁰ Figure 3.

2.2. Two dimensional fast conduction Purkinje

The Purkinje network in humans and other mammals is distributed in a layer within the subendocardium, which is thin with respect to the myocardium thickness (of the order of 0.5–100 μm [56] compared to an average thickness of ¹⁹⁵ 7±1 and 15.4±2.3 mm for the right and left ventricles, respectively [57]) and is made of thicker fibers with a branching distance of the order of 2 mm [58] which bifurcate multiple times until forming a dense plethora of thinner fibers [47, 59]. This dense network of fibers is typically mimicked in computational models through the growth of a fractal structure by defining a set of generating rules
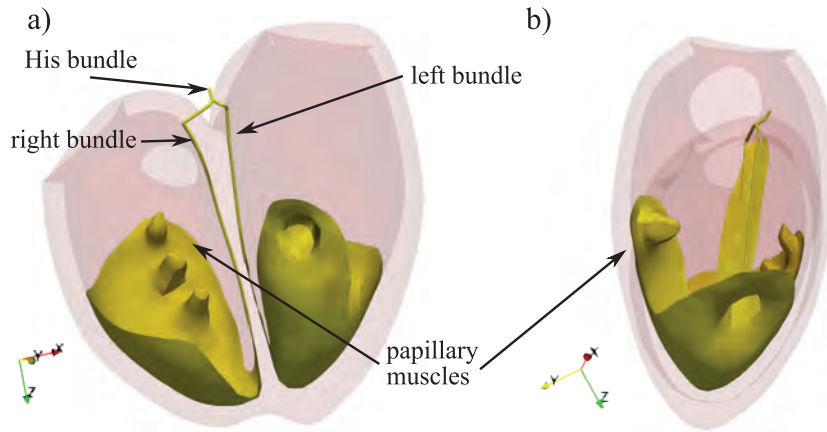
9

Figure 4: Ventricular bundles and Purkinje network, which cover the papillary muscles.

and an initial topology (in a similar fashion to the growing models for plant branches) with the smallest branching structure in the order of 100 μm [47, 12, 13]. As an alternative approach to the growth of a fractal 1D network, the dense fiber distribution of the Purkinje network is here merged into a continuum 2D isotropic conductive medium wrapping the endocardium. Such approach is motivated by the uncertainty on the precise arrangement of Purkinje fibers and the great variability among individuals, which make it difficult to develop an accurate fractal rule for the network growth. Furthermore, a high fiber density (more than 2000 branches and 300 PMJs for the major bundles [60] and an even smaller branching distance of 0.1–2 mm for thinner branches [58, 47]) is required to adequately model the Purkinje and correctly activate the myocardium both in healthy [48] and pathologic [43] cases. Figure (4) shows as the 2D Purkinje network develops from the His bundle and extends parallel to the left and right bundles until reaching the apex of the heart and then raises up upon two third of the ventricles height, completely covering the papillary muscles in order to timely activate their contraction at early systole. The right and left sides of the Purkinje complex do not have a direct electrical connection since they are separated by the thickness of the interventricular septum.

2.3. Three dimensional excitable myocardium

The 3D myocardium is made of three excitable and conductive media, namely two for the left and right atria and another for the ventricles (see Figure 2d), which has been built using modeling software so as to reproduce high–resolution clinical images and medical atlas. This splitting of the myocardium is inspired by the cardiac electrophysiology as the heart septum between the atria and the ventricles (the fibrous trine plane) acts as an electrical insulator, thus decoupling the atrial and the ventricular electrophysiology. The transmembrane depolarization front, indeed, only propagates from the atria to the ventricles through the AV–node that is part of the 1D network of bundles (see § 2.1). Similarly, the atria are electrically insulated by the atrial septum and they can thus be modelled as two disjoint electrical domains. On the other hand, the ventricular myocardium cannot be further subdivided into two independent meshes as, we anticipate, the ventricular endocardium is made by the same muscular fibers wrapped around the ventricles which are thus electrically connected [29].
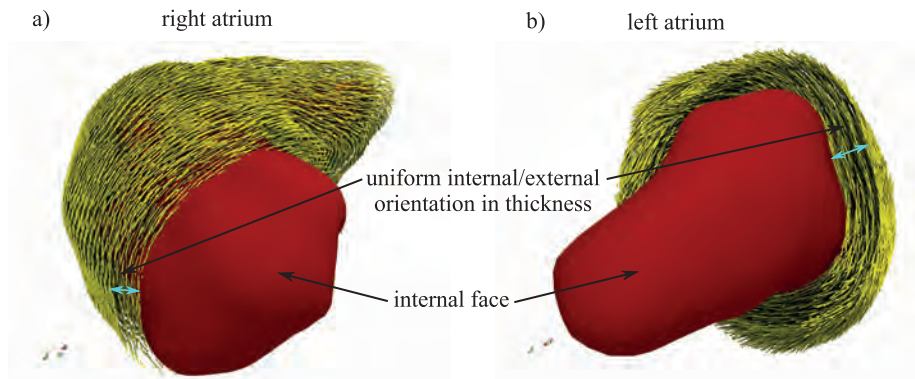

Figure 5: Fibers orientation in the a) right and b) left atrium. The red surface indicate the internal endocardium.

Figure 5 shows the muscular fibers orientation within the (a) right and (b) left atrial wall, with the fibers wrapping around the main atrial axes as observed in–vivo by diffusion tensor magnetic resonance [8]. Since the atrial fiber orientation is uniform within the myocardium thickness (of about 4 mm), this is first

11

defined on the atrial endocardium (red surfaces in Figure 5) and, then replicated, at each cell across the 3D myocardium thickness. Different or patient–specific fiber orientation in healthy and pathological conditions can be included as well in the geometrical description of the 3D media.
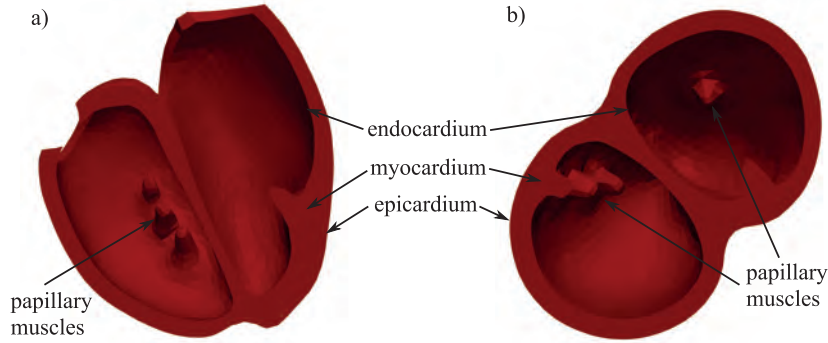

Figure 6: a) Front and b) top view of the ventricular myocardium incorporating the papillary muscles.

240

The ventricular myocardium is modelled as a single 3D mesh for both the left and right ventricles and includes the papillary muscles, whose location corresponds to the most recurrent one observed in a population study [61, 62]. The main reason for creating a single mesh (instead of two as in the modelling of the atria) is that the external part of the ventricular myocardium wrapping the whole heart (often described as a *scarf* [19]) is electrically connected and allows for a slow propagation of the depolarization front from one ventricle to the other, which is not observed in healthy cases as the two ventricles are simultaneously activated by the right and left fast conduction branches but it may occur in pathologic cases as studied in the next section.

Although the orientation of the muscle fibers shows some variability among individuals, it is known to vary across the myocardium wall from $\alpha_{epi} = 60°$ at the endocardium to $\alpha_{endo} = -60°$ at the epicardium with respect to the ventricles major axis [20, 63, 64]. The vector field, corresponding to the fibers orientation at each cell of the 3D mesh, is thus defined as $\alpha = \alpha_{endo} \cdot d + \alpha_{epi} \cdot (1-d)$,
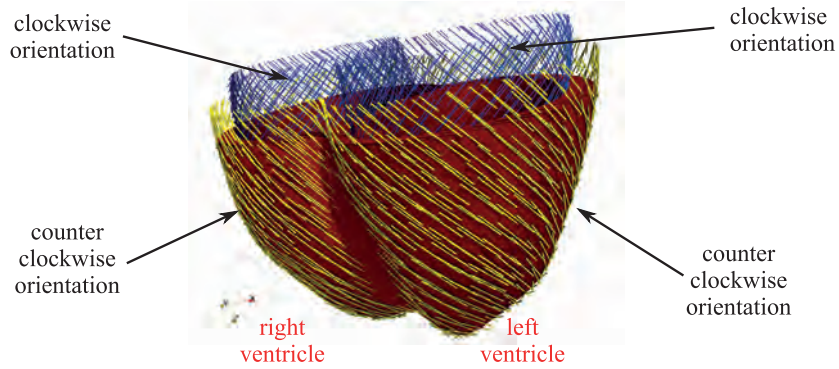
12

Figure 7: Fibers orientation in the ventricular myocardium. The external (yellow) epicardial muscular fibers are oriented in opposite direction compared with the internal endocardial one (blue).

where d is the cell transmural distance from the endocardium normalized by the myocadium thickness (of about 8 mm on average), yielding the typical counter-clockwise (clockwise) fiber orientation over the epicardium (endocadium) shown in Figure 7.

3. Governing equations and numerical method

3.1. The bidomain model

The electric wave propagating across the cardiac tissue is governed by the bidomain model that is made by the following system of two reaction–diffusion PDEs, coupled with a set of nonlinear ODEs corresponding to the cell model:

$$\chi \left(C_m \frac{\partial v}{\partial t} + I^{ion}(v, \mathbf{s}) + I^s \right) = \nabla \cdot (M^{int} \nabla v) + \nabla \cdot (M^{int} \nabla v^{ext}),$$

$$0 = \nabla \cdot (M^{int} \nabla v + (M^{int} + M^{ext}) \nabla v^{ext}), \quad (1)$$

$$\frac{\mathrm{d}\mathbf{s}}{\mathrm{d}t} = F(v, \mathbf{s}).$$

Here, v and v^{ext} are the unknown transmembrane and extracellular potential (expressed in mV), whereas the surface–to–volume ratio of cells $\chi = 140$ mm^{-1} and the specific membrane capacitance $C_m = 0.01 \mu$F mm^{-2} are set as in [65].

13

M^{int} and M^{ext} are the conductivity tensors of the intracellular and extracellular media that depend on the local fiber orientation with a faster propagation velocity along the fiber than in the orthogonal directions. In the case of a 3D conductive media as the myocardium these tensors have rank three and are diagonal when expressed in the fiber ($\|$), sheet–fiber ($/$) and cross–fiber ($\perp$) directions [29], see Figure 7:

$$\hat{M}^{ext} = \begin{bmatrix} m_{\|}^{ext} & 0 & 0 \\ 0 & m_{/}^{ext} & 0 \\ 0 & 0 & m_{\perp}^{ext} \end{bmatrix}, \qquad \hat{M}^{int} = \begin{bmatrix} m_{\|}^{int} & 0 & 0 \\ 0 & m_{/}^{int} & 0 \\ 0 & 0 & m_{\perp}^{int} \end{bmatrix}. \qquad (2)$$

The conductivity tensor in the global coordinate system are thus obtained by the transformations

$$M^{ext} = \mathcal{A}\hat{M}^{ext}\mathcal{A}^{T}, \qquad M^{int} = \mathcal{A}\hat{M}^{int}\mathcal{A}^{T}, \qquad (3)$$

where $\mathcal{A}$ is the rotation matrix containing column–wise the components of fiber, sheet–fiber and cross–fiber normal unit vectors. On the other hand, for 2D electrical media as the Purkinje model, the transmembrane potential depolarization can only propagate in the fiber and sheet–fiber directions corresponding to the principal conductivities $m_{\|}^{ext,int}$ and $m_{/}^{ext,int}$. Lastly, in the case of 1D conductive media as the fast conduction network of bundles, the conduction properties are only given by the fiber conductivity $m_{\|}^{ext,int}$.

The last of equations (1) indicates a set of nonlinear ordinary differential equations (ODEs) governing the cellular-scale dynamics in the bidomain equations. Its complexity depends on the physiological details of the model and the unknown state vector, $\mathbf{s}$, couples the cell model with the bidomain equations through the ionic current per unit cell membrane area I^{ion}. Since the various components of the cardiac electrophysiology system have different cellular properties yielding different ionic fluxes and, consequently, different action potential profile, we adopt a Courtemanche cell model [1] for the atrial myocytes (and the corresponding internodal pathways), a Stewart model [2] for the Purkinje network and a ten Tusscher–Panfilov model [3] for the ventricular myocytes.

14

These cell models are made by a system of 21, 20 and 19 ODEs, respectively, which are not reported here for the sake of brevity.

The ionic current, I^s gives to a periodic electrical stimulus concentrated in time and space at the SA–node triggering the electrical stimulus to the ventricular myocardium, thus initiating the electrical depolarization throughout the heart:

$$I^s = S_a(\mathcal{H}[t] - \mathcal{H}[t - S_d]), \tag{4}$$

where $S_a = 1 \ mA/mm^2$ and $S_d = 2.5 \ ms$ are the stimulus amplitude and duration, t is the time within a heart beat and $\mathcal{H}[\cdot]$ the Heaviside function. In a previous work, we have verified through an uncertainty quantification analysis that the values of the amplitude and duration of the stimulus do not significantly impact the subsequent depolarization of the fast conducting bundles, as far as they vary in physiological ranges [66].

3.2. Numerical method

The set of governing equations (1) is solved using an in–house finite volume (FV) library, which provides a suitable approach for solving the electrophysiology equation in complex geometries. As introduced above, the cardiac electrophysiology media is split in a 1D graph for the fast conduction bundles, a 2D shell for the fast conduction Purkinje and 3D media for the atrial and ventricular myocardium, which are respectively segmented with linear, triangular and tetrahedral elements.

Using the divergence theorem, the bidomain equations (1) can be rewritten in conservative form on each grid cell, Ω_i,

$$\int_{\Omega_i} \chi \left(C_m \frac{\partial v}{\partial t} + I^{ion} + I^s \right) d\Omega = \int_{\partial \Omega_i} (M^{int} \nabla v) \cdot \mathbf{n} d\gamma + \int_{\partial \Omega_i} (M^{int} \nabla v^{ext}) \cdot \mathbf{n} d\gamma,$$

$$0 = \int_{\partial \Omega_i} [M^{int} \nabla v] \cdot \mathbf{n} d\gamma + \int_{\partial \Omega_i} [(M^{int} + M^{ext}) \nabla v^{ext})] \cdot \mathbf{n} d\gamma,$$

$$\tag{5}$$

where $\mathbf{n}$ is the normal unit vector of the cell boundary, $\partial \Omega_i$.
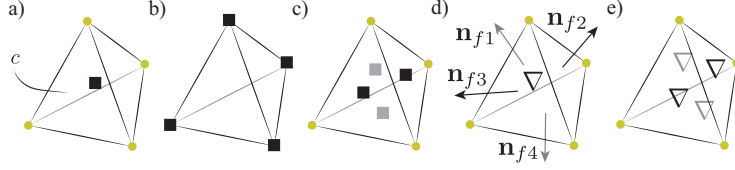
Figure 8: Graphical scheme of the procedure to evaluate the gradient at the cell faces of a 3D media. a) The cell—based v_c is interpolated to obtain b) the node–based v_n, which is then used to estimate the same quantity at c) the midpoint of the tetrahedrons faces, v_f. The latter is used to determine d) ∇v_c on the cell center using the Gauss–Green theorem and is successively interpolated to evaluate the e) gradient at the mesh faces ∇v_f.

In the case of the 3D myocardium, the domain is discretized through a tetrahedral mesh and equation (5) for a cell based FV method reads

$$\chi \left(C_m \frac{\partial v_c}{\partial t} + I_c^{ion} + I_c^s \right) V_c = \sum_{j=1}^{4} A_{fj} [M_{fj}^{int} (\nabla v_{fj} + \nabla v_{fj}^{ext})] \cdot \mathbf{n}_{fj},$$

$$\sum_{j=1}^{4} A_{fj} [M_{fj}^{int} \nabla v_{fj}] \cdot \mathbf{n}_{fj} + \sum_{j=1}^{4} A_{fj} [(M_{fj}^{int} + M_{fj}^{ext}) \nabla v_{fj}^{ext}] \cdot \mathbf{n}_{fj} = 0,$$

(6)

where the subscript c indicates that the quantities are evaluated at the cell center whereas the subscript fj denotes the $j - th$ face of the cell c. In the case the external and the internal conductivity tensors are parallel $M^{ext} = \lambda M^{int}$ the bidomain model (6) reduces to the monodomain equation (6):

$$\chi \left(C_m \frac{\partial v_c}{\partial t} + I_{ion,c} + I_{s,c} \right) V_c = \sum_{j=1}^{4} A_{fj} [M_{fj} \nabla v_{fj}] \cdot \mathbf{n}_{fj}, \qquad (7)$$

where $M = \lambda M^{int} / (1 + \lambda)$.

The fluxes over the tetrahedron cell faces are evaluated as indicated in reference [67] and summarized in Figure 8. Firstly, the transmembrane potential at the vertex nodes v_n (see panel 8 b) is computed by using the weighted average of the potential within the cells surrounding that node, v_k, yielding $v_n = \sum_{k=1}^{Nc_n} v_k d_k^{-1} / \sum_{k=1}^{Nc_n} d_k^{-1}$, where N_{c_n} is the number of cells sharing the node and d_k is the distance between the node and the k–th cell center. Once the values v_n are found, the values of the transmembrane potential at the faces centroids v_f (see panel 8 c) are calculated by averaging the three nodal values

at the triangle vertices. According the Gauss–Green formula (panel 8 d), the gradient of the transmembrane potential ∇v_c is related to the flux of the same quantity through the cell faces and, using a second order accurate mid-point integration rule to evaluate these fluxes, we get $\nabla v_c = \frac{1}{V_c} \sum_{j=1}^{4} v_{fj} S_{fj} \mathbf{n}_{fj}$, where V_c is the volume of the cell and v_{fj}, S_{fj}, $\mathbf{n}_{fj}$, are the transmembrane potential, area and the normal vector at j–th face. The gradient at the mesh faces is then obtained as the weighted average of the cell gradients defined at the cells c_1 and c_2 sharing the face f, $\overline{\nabla v}_f = \alpha_{c_1} \nabla v_{c_1} + \alpha_{c_2} \nabla v_{c_2}$, where α_{c_1} and α_{c_2} are the linear interpolation weights defined on the position of the face f with respect to the centers of the two cells ($\alpha_{c_1} + \alpha_{c_2} = 1$). The resulting face gradient $\overline{\nabla v}_f$ is computed not only using the two transmembrane potential values defined at the two cells sharing the face, but also using the cell values of all the cells sharing the nodes of the two cells c_1 and c_2, thus enlarging the stencil of the formula. The 3D face gradient $\overline{\nabla v}_f$, can be modified in such a way to include the low–stencil directional derivative

$$\nabla v_f = \overline{\nabla v}_f + \left[\frac{v_{c_1} - v_{c_2}}{d_{c_1 c_2}} - \left(\overline{\nabla v}_f \cdot \mathbf{e}_{c_1 c_2} \right) \right] \mathbf{e}_{c_1 c_2}, \qquad (8)$$

270 where $\mathbf{e}_{c1c2}$ is the unity vector in the direction joining the centroid of the two cells c_1 and c_2 straddling the face. Such treatment of the cross diffusion term of the face gradient (which is often used to improve the stability of the method in the case of implicit schemes through a deferred correction [67]) reduces to the second–order difference quotient between c_1 and c_2 when $\mathbf{e}_{c1c2}$ is parallel to

275 the face normal vector, $\mathbf{n}_f$; as is the case for orthogonal or locally orthogonal grids. The face gradient (8) (corresponding to the last panel in Figure 8) can be then directly used to compute the fluxes in the conservative equation (1) and obtain the spatially discretized bidomain equations in the 3D myocardium. A similar FV approach is used to discretize the bidomain/monodomain equations

280 over 1D and 2D media (in order to model the bundles and Purkinje network, respectively) with the only exception that a vertex–based FV is used in the 1D case so to better handling multiple bundles branching from the same grid node, as happening at the internodal pathway and at the Bachmann's bundle (see

17

Figure 3).

This FV approach thus provides an effective spatial discretization of the bidomain equations over complex geometries and is second–order accurate in space provided the grid is sufficiently regular (see the convergence analysis in section 4). Importantly, as typical in FV methods the mass matrix is diagonal, thus meaning that in the case of an explicit time scheme, the discretized unsteady bidomain equation for v (as well as the monodomain one) can be marched in time simply correcting the transmembrane potential at the previous timestep by summing an incremental vector. Although an explicit temporal scheme needs a timestep small enough to prevent numerical instabilities, still the overall computational cost is smaller than that of an implicit scheme which requires the solution of a nonlinear system at each mesh element and any timestep owing to the nonlinearity of the cell model. However, the cell models are extremely stiff, due to the significant variables variations over short timescales of the spike–and–dome of the action potential and of the so–called gating variables (describing the opening and closing dynamics of ion channels) and require prohibitively small timesteps to assure numerical stability. This difficulty can be circumvented by noting that the ODEs governing the gating variables are quasi-linear and can be solved analytically within a timestep if the transmembrane potential v is held constant, whereas an explicit method is used to integrate the remaining nonlinear ones. This semi–analytical approach is known as the Rush–Larsen scheme [68, 69] and it has been successfully applied to the three cell models adopted here: the Courtemanche model with 15 gating variables out of 21 state variables, the Stewart model with 13 gating variables out of 20 state variables and the ten Tusscher–Panfilov models with 13 gating variables out of 19 state variables. The enhanced stability properties of the method thus allow for an integration timestep more than one order of magnitude larger than the one used with a standard explicit time scheme.

On the other hand, owing to the first order accuracy of the Rush–Larsen solution, the non–gating variables of the cell model (typically describing the variations of intracellular ions concentrations) and the spatially discretized bidomain

18

equations (6) are integrated in time using a forward Euler method [69] and at each timestep the updated transmembrane potential $v(t^{n+1})$ is thus obtained as an explicit function of v, v^{ext}, I^{ion} and I^s previously computed at time t^n and, similarly, the updated state vector of the cell model $\mathbf{s}^{n+1}$ is computed using $\mathbf{s}^n$. As the numerical converge analysis (see section 4) reveals that the error of the numerical solution is more sensitive to the spatial rather than to the temporal refinement, the Rush–Larsen method with its remarkable stability properties is thus a convenient temporal scheme for the bidomain/monodomain model, although first order accurate. Furthermore, in the perspective of multi-physics heart simulations including the coupled structural and blood dynamics, the timestep will be limited to few μs by the fluid–structure–interaction [41] and a first order temporal scheme for the electrophysiology system entails a numerical precision of the solution with such a small timestep. In the case of bidomain model, once $v(t^{n+1})$ is solved, the external potential $v^{ext}(t^{n+1})$, is obtained by solving the linear system given by the second equation of the system (6) through an iterative GMRES method with restart [70] using the external potential computed at previous time, $v^{ext}(t^n)$, as first estimate for the unknown field $v^{ext}(t^{n+1})$.

The FV library has been GPU accelerated using CUDA Fortran [71] which extends Fortran by allowing the programmer to define Fortran functions, called kernels, which when called are executed N times in parallel by N different CUDA threads, as opposed to the serial nature of the regular Fortran functions, thus greatly improving the performance. Furthermore, CUDA provides CUF kernel directories which automatically run single and nested loops on the GPU device without neither modifying the original CPU code nor writing a dedicated GPU subroutine. Specifically, the electrophysiology solver results in a sequence of loops on the mesh cells and on the mesh faces, which are GPU accelerated simply wrapping the original CPU code in the CUF kernel directive.
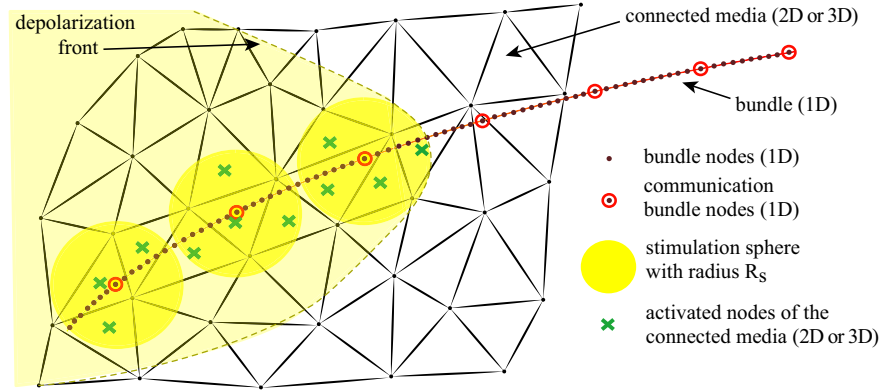
Figure 9: Sketch of electrical coupling between the 1D fast conduction bundles and the surrounding 2D (or 3D) mesh. The wave front of the electric potential propagates across 1D mesh causing the threshold values of the communication nodes to be exceeded, thus activating the 2D (or 3D) cells within a radius R_s.

3.3. Subsystems coupling

The topological splitting of the cardiac electrophysiology network requires a coupling mechanisms to connect electrically the various subdomains. In particular, three two–way couplings are needed: (i) a first one between the 1D bundles and the 2D Purkinje networks, (ii) another between the 1D network of bundles and the 3D atrial myocardium and (iii) a last one between the 2D Purkinje and the 3D ventricular myocardium.

As sketched in Figure 9, the communication between the 1D mesh and the underlying 2D (or 3D) counterpart occurs through some communication nodes (CNs, indicated by red circles) which are defined in the preprocessing phase as a subset of the bundle grid nodes (black dots). In particular, as the transmembrane potential at a CN exceeds a certain threshold (here set to 0 mV), an external localized stimulus I^s (with $S_a = 1\ mA/mm^2$ and $S_d = 0.5\ ms$, see equation (4)) is applied to the underlying 2D (or 3D) mesh cells within a distance R_S from the CN, thus initiating a depolarization front in the 2D (or 3D) media. Specifically, since the 1D domain represents the network of internodal pathways that are some millimeters thick in the atrial myocardium [7], the

20

communication range for the coupling between the 1D and the 3D atrial mesh is taken equal to $R_S = 1$ mm, whereas any CNs between the 1D and the 3D ventricular mesh are not present since the bundles do not directly excite the ventricular myocardium (they are isolated by fibrous sheaths) but they only transfer the propagation front to the Purkinje network [72]. Hence, the depolarization of the Purkinje mesh is initiated by the CNs between the 1D and the 2D domains having a smaller communication range of $R_S = 0.1$ mm, scaling as the local Purkinje thickness. Although all bundle nodes (black dots in Figure 9) can be taken as CNs, only a subset of them is used in order to reduce the computational cost of the coupling since at any timestep the local transmembrane potential at the CNs should be monitored for eventually applying a localized electrical stimulus. In this work, the CNs are equally distributed over the 1D network with a relative distance among them of $\varsigma \cdot \tau \approx 1$ mm, where $\varsigma = 2$ m/s is the typical internodal pathways propagation speed and $\tau = 0.5$ ms is the maximum time delay in the activation between two consecutive CNs, which is found to trigger correctly the depolarization of the Purkinje network as later shown in section 5.1. On the other hand, a shorter τ would correspond to a denser distribution of the CNs and vice–versa.
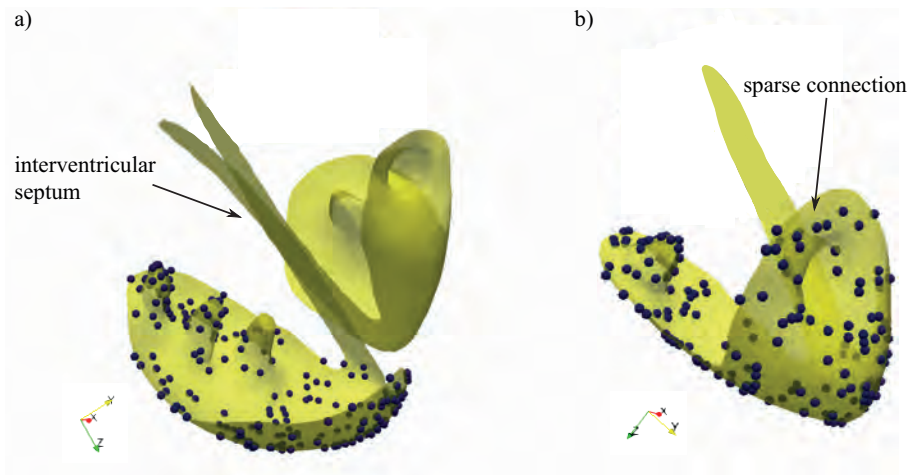

Figure 10: Distribution of the communication nodes (CNs) between the 2D Purkinje and the 3D ventricular myocardium, corresponding to the Purkinje muscle junctions (PMJs).

21

Figure 10 show the distribution of the CNs between the 2D and the 3D ventricular media ($R_S = 0.1$ mm), which allow the Purkinje network to activate the ventricular myocardium with an orthodromic delay of 5 milliseconds [14]. The density and the positions of these CNs is user–defined and it has been set so to reproduce the ones of the Purkinje muscle junctions (*PMJ*) [60, 73]. In this work 300 CNs equally distributed among the left and right ventricles [74] have been considered with their distribution corresponding to the one of the PMJ with no CNs present in the interventricular septum as the Purkinje network is insulated by fibrous sheaths in that region [75, 72] (Figure 10 a).

In the case of healthy cardiac electrophysiology, the electrical coupling through the CNs is *one–way*, meaning that only the lower topological domain triggers an electrical stimulus on the higher one, e.g. the 1D bundle excites the 3D myocardium but not vice–versa. On the other hand, in some pathological cases such as nodal re-entry tachycardia [76] or antidromic propagation (re–enter of the signal in the Purkinje network from the myocardium) [14], the coupling is *two–way* and the 3D myocardium can eventually excite back the 1D bundles and the 2D Purkinje, as shown in § 5.

4. Numerical convergence and validations

The convergence of the numerical method is investigated using a procedure similar to the one reported in the benchmark paper [65] by solving the monodomain and the bidomain equations over a 3D Cartesian domain of size $20 \times 7 \times 3$ mm^3 coupled with the ten Tusscher–Panfilov cell model [3]. In order to validate the 2D and 1D solvers, a similar test–case is also run on a rectangular 2D domain (20×7 mm^2) and on a straight linear domain (of length 20 mm). In all cases, the Cartesian domain is discretized by a structured grid with a minimum grid size of 0.5, 0.2 and 0.1 mm in each direction (x in the 1D, x, y in the 2D and x, y, z in the 3D), and three different timesteps have been used, namely 0.05, 0.01 and 0.005 ms. The muscle fibers are taken aligned with the long axis direction (20 mm in 2D and 3D) and the electrophysiology
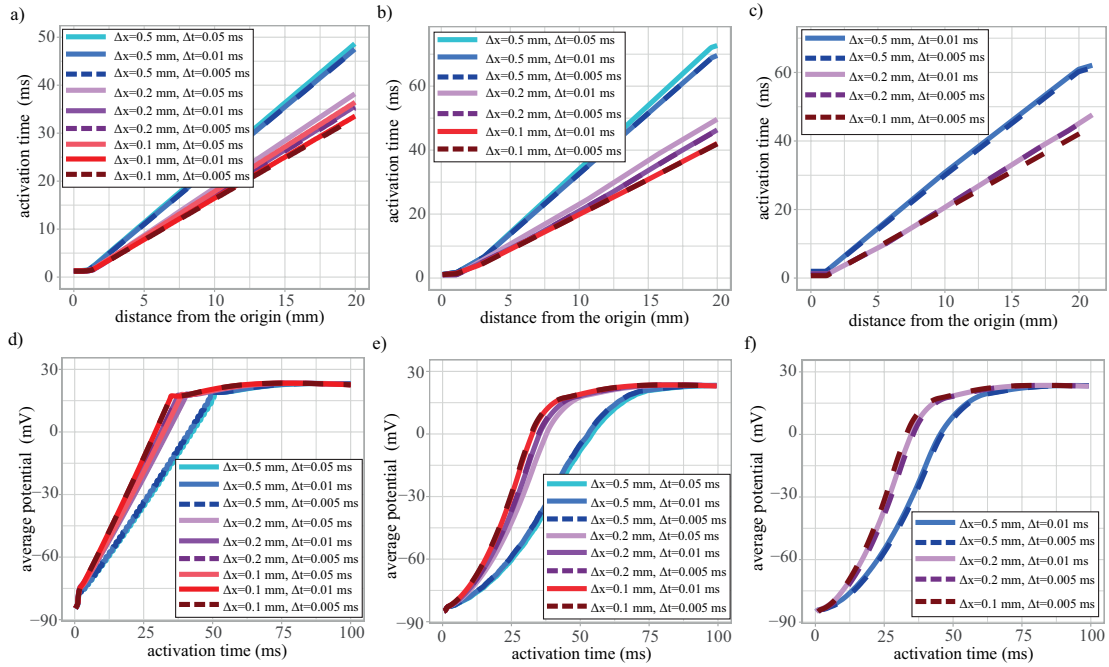
22

Figure 11: Activation time along the main diagonal in the a) 1D, b) 2D and c) 3D domain according to the monodomain model for various temporal and spatial resolutions (Δx is the grid spacing the x direction in 1D, x, y in 2D and x, y, z in 3D). The corresponding average transmembrane potential is reported in d), e) and f), respectively.

parameters, including the initial state variables of the cell model, are set as in [65]. The initial stimulus is applied within a line/square/cube of side 1.5 mm placed in the corner closer to the origin.

In the case of the monodomain solver, Figure 11 reports the activation time (defined as the instant when the transmembrane potential exceeds 0 mV) along the diagonal of the domain departing from the corner where the stimulus is applied for the (a) 1D (b) 2D and (c) 3D domains. The corresponding transmembrane potential averaged in the domain volume V, $\overline{v}(t) = \int_V v(\mathbf{x}, t)dV/V$ are reported as a function of time in Figure 11(d,e,f), showing that, as the spatial grid is refined, the propagation speed of the depolarization front increases until convergence is attained for the more refined grid spacing with a timestep equal–smaller than $\Delta t = 0.01$ ms. The corresponding convergence curve for the
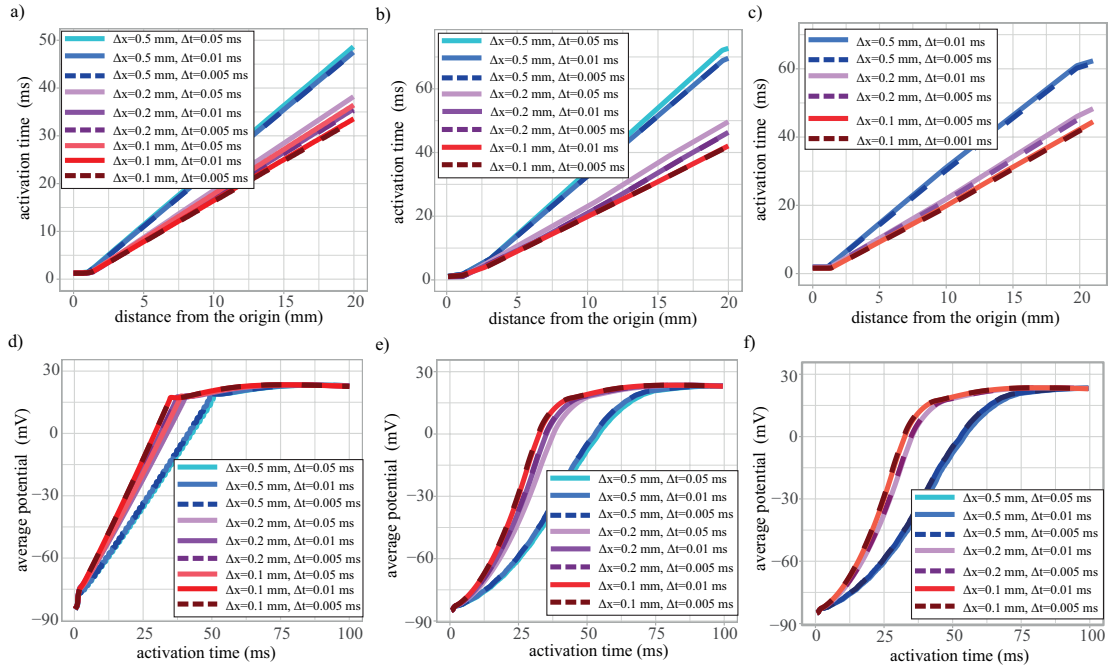
23

Figure 12: Same as Figure 11 but solving the bidomain electrophysiology model.

bidomain model are given in Figure 12 for each topological dimension of the conductive media, thus showing similar results for the same grid spacing and

420 timestep.

In the 3D case, the numerical solution of the monodomain and bidomain equations can be validated against previous results from the literature. The former is validated against the benchmark paper of Niederer et al. 2011 [65] where 11 different numerical codes (either based on finite elements or finite differences)

425 have been used and the resulting average activation time along the diagonal of the cubic domain (blue solid line) and standard deviation (blue shaded region) are reported in Figure 13 (a). Moreover, the solution of the bidomain equations is validated against the results of Cuccuru et al. [78], which is reported in Figure 13 (b) for different spatial steps and different polynomial degrees, see [78]

430 for further details on their numerical method. Both the monodomain and the bidomain results obtained with our numerical solver fit well those reported in
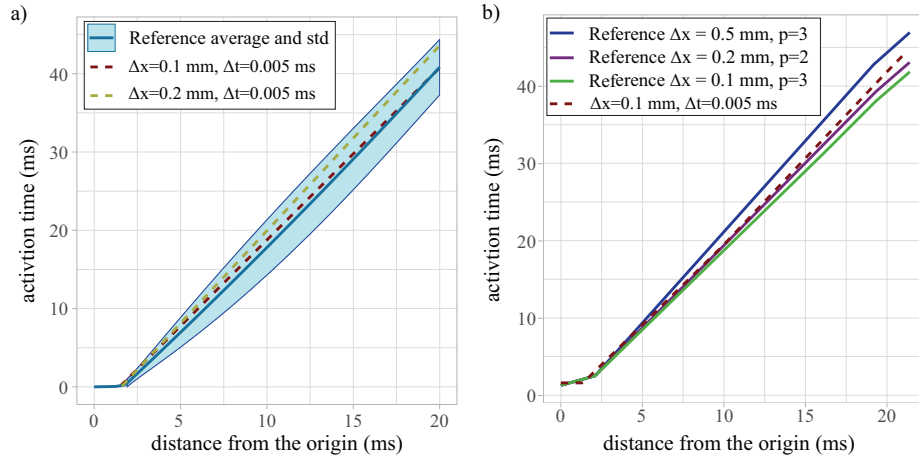
24

Figure 13: Average transmembrane potential in the 3D domain according to a) the monodomain and b) the bidomain electrophysiology model. a) Our numerical results (yellow dashed line for $\Delta x = 0.2$ mm and red dashed one for $\Delta x = 0.1$ mm) are compared against the average results (blue solid line) of the benchmark paper [77], where the shaded area indicates the corresponding standard deviation. In panel b) our code is validated against the results reported [78].

the literature.

The corresponding convergence curves are reported in Figure 14 in the case of the 1D, 2D and 3D monodomain model. Figure 14(a) indicates the second order spatial accuracy of the FV method by showing the error on the average transmembrane potential over the domain at time $t = 50$ ms (and timestep set to $\Delta t = 0.005$ ms) as a function of the average grid size, $\overline{\Delta x}$. On the other hand, Figure 14(b) reports the same quantity (evaluated with $\overline{\Delta x} = 0.31$ mm) as a function of the timestep Δt, thus retrieving the first order temporal accuracy of the Rush–Larsen temporal integration scheme, where the non–gating variables are solved using forward Euler. The numerical error could be reduced by adopting a second–order Adams–Bashforth scheme for the non–gating variables (dashed blue line for the 1D case), although a modified second order Rush–Larsen scheme [79] would be needed to attain a second order accuracy.

Table 1 reports the wall–clock time for solving a single bidomain and mon-
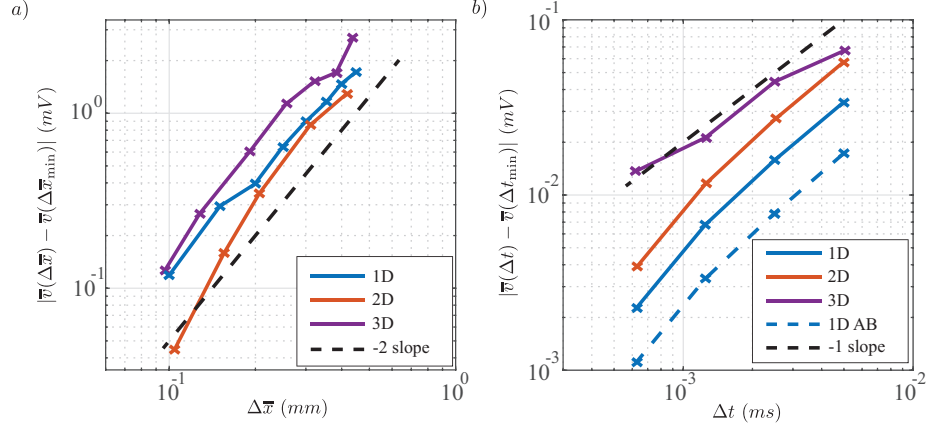
25

Figure 14: (a) Spatial and (b) temporal convergence curves of the 1D, 2D, and 3D monodomain solver. In (a) the error on the average transmembrane potential (computed at time $t = 50$ ms for $\Delta t = 0.005$ ms) is shown as a function of the mean grid size, $\overline{\Delta x}$. In (b) the same quantity (at time $t = 50$ ms for $\overline{\Delta x} = 0.31$ mm) is reported as a function of the timestep, Δt.

Grid Δx, cells	CPU bidomain	GPU bidomain	speedup bidomain	CPU monod.	GPU monod.	speedup monod.
0.5 mm, 20'160	0.027 s	0.0015 s	18	0.018 s	0.0002 s	90
0.2 mm, 315'000	0.45 s	0.017 s	27	0.20 s	0.0013 s	154
0.1 mm, 2'520'000	3.7 s	0.09 s	41	1.6 s	0.009 s	177

Table 1: Wall–clock time for integrating a single bidomain and monodomain time step for the three Cartesian grids considered in Figures 11–13. The CPU time is obtained using a single core Intel(R) Xeon(R) Gold 6230 with 2.10GHz, whereas the GPU time corresponds to a Tesla V100 from Nvidia.

odomain timestep on the benchmark Cartesian domain using a single CPU core or GPU device. Running the GPU version of the code yields a significant speedup in all cases, which increases as the grid gets more refined owing to the better balance of workload across the GPU threads running in parallel. It can be observed, that the speedup is larger in the case of monodomain computations

450

26

with respect to the bidomain counterpart because the Arnoldi iteration and the solution of the corresponding Hessenberg system in the GMRES algorithm are based on the Lapack library running on the CPU.

The convergence of the numerical solution over the cardiac domains used in sections 2 and 5 for the electrical conductivities reported in Table 2 is assessed by monitoring the average transmembrane potential as a function of time, $\bar{v}(t)$. Figure 15(a) shows $\bar{v}(t)$ solved over the 1D network of fast conduction bundles using the monodomain model coupled with the Courtemanche cell model with a timestep equal to $\Delta t = 0.001$ ms, thus showing good convergence for a spatial discretization finer than $\Delta x = 0.25$ mm (corresponding to a number of cells equal to $2'000$). On the other hand, the monodomain equations over the right Purkinje 2D media coupled with the Stewart cell model are at convergence for the number of triangles of about 54'000 (i.e. $\Delta x = 0.45$ mm). The bidomain solution over the 3D left atrium becomes grid independent for a number of cells around 5'500'000 ($\Delta x = 0.31$ mm), but a coarser grid with 1'500'000 cells (corresponding to $\Delta x = 0.53$ mm) yields a slower propagation of the depolarization front corresponding to a time delay of the electrical activation of the chamber below 3.5% the heart beating period (equal to 750 ms for a heart rate of 80 b.p.m.). Based on these results, a 1D grid made of 2'500 linear elements and a 2D grid of 108'000 triangles have been used to discretize the fast conduction and the Purkinje networks with a timestep of 0.0001 ms. Hence, the electrophysiology of the 3D myocardium is integrated with a timestep of $\Delta t = 0.005$ ms using using 1'500'000, 2'500'000 and 5'500'000 tetrahedra for the left atrium, right atrium and ventricles, respectively. The electrophysiology of each 3D chamber is integrated using a dedicated GPU card Tesla V100 from Nvidia and the wall–clock time to run a single heart beat is thus given by that of solving the ventricular electrophysiology, which is equal to 7.9 hours (corresponding to a speedup of 60 times with respect to the serial CPU version of the code). Remarkably, since the computational cost is dominated by the 3D solution of the bidomain equations, it can be greatly reduced by using a monodomain approach as it avoids solving a large linear system for v^{ext}, thus
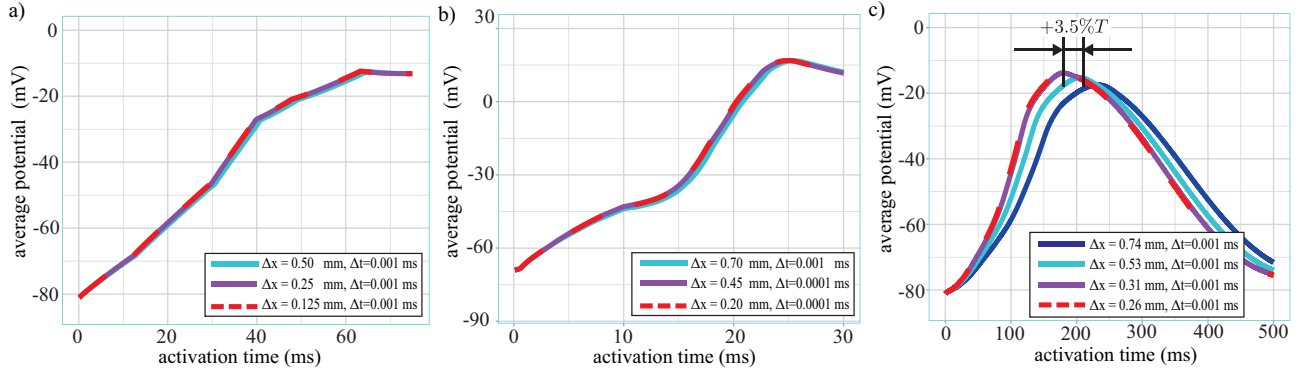
27

Figure 15: Average transmembrane potential for different temporal and spatial resolutions over the a) the internodal pathways, b) the right Purkinje network and c) the left atrium. In the 3D case, a spatial resolution of $\Delta x = 0.53$ mm corresponds to a delay in the chamber activation below $3.5\%T$, where T is the heart beating period which is equal to 750 ms for a heart rate of 80 b.p.m..

obtaining a wall–clock time of 1.4 hours per heart beat.

5. Results: electrophysiology of the whole heart

The electrophysiology of the whole heart is solved using the cardiac configuration introduced in § 2 (Figure 2), which is composed of a 1D network of bundles, a 2D surface to mimic the Purkinje placed at the ventricular endocardium and 3D media for atrial and ventricular myocardium. In order to better account for their heterogeneous electrophysiology properties three different cell models are adopted (Figure 16). In particular, the Courtemanche model [1] is used for the atrial bundles and myocardium, which has a resting potential of -80 mV and is characterized by rapid repolarization occurring in about 200 ms. On the other hand, the high peak of depolarization followed by a stable plateau phase of about 250 ms observed in the Purkinje cells is modelled through the Stewart cell model [2], whereas the ionic fluxes across the ventricular myocytes are governed by the ten Tusscher–Panfilov cell model [3] exhibiting a resting potential of about -85 mV and a longer depolarization plateau of about 300 ms which is related to a longer muscular contraction of the fibers. Furthermore, the depolar-
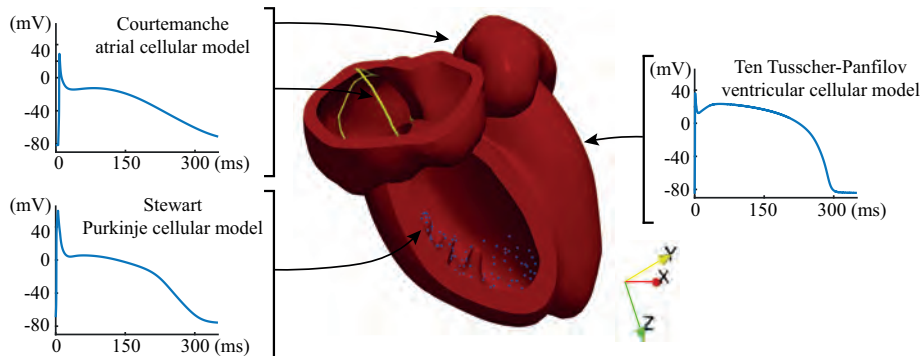
28

Figure 16: Action potential at different cardiac locations. a) The Courtemanche cell model [1] is used in the 1D atrial bundles and in the 3D atrial myocardium, b) the Stewart model [2] is adopted for the Purkinje network and c) the ten Tusscher-Panfilov model [3] governs the action potential in the 3D ventricular myocardium.

ization front propagates at different velocity through these media according to different electrical conductivities, which have been set in the electrophysiology

500 model as summarized in Table 2. Since the monodomain and bidomain models are equivalent in the case of a 1D domain, only a single electrical conductivity has been set so to reproduce the propagation velocity reported in the literature [5]. Owing to the high density of the Purkinje fibers and their heterogeneous intracellular and extracellular orientation, the Purkinje network is modelled as

505 a uniform media governed by the monodomain equation with an isotropic conductivity tensor with its components set to reproduce a propagation velocity of 4 m/s [66, 80, 6]. The intracelluar and extracellular electrical heterogeneity in the 3D ventricular myocardium is accounted by setting an anisotropic conductivity tensor in the bidomain equations as reported in the literature [65]

510 (Table 2). Owing to the lack of data on the atrial myocardium conductivity, the same conductivity tensors as in the ventricles have been used but rescaled by a factor to match the propagation velocity measured experimentally.

5.1. Healthy electrophysiology

We can now analyze the whole cardiac electrical activation in a healthy

515 heart. Figure 17 shows the depolarization of the fast conduction atrial bundles

29

heart component	cell/PDE model	conductivity (mS/mm)	reference
1D internodal bundles	Courtemanche, isotropic monodomain	$m_\parallel = 1.29$	corresponding to a velocity 1.54 m/s [6, 80, 66]
2D Purkinje network	Stewart, isotropic monodomain	$m_\parallel = m_/ = 3.95$	corresponding to a velocity 4.0 m/s [5]
3D ventricles	ten Tusscher–Panfilov, bidomain	$m_\parallel^{ext} = 0.62$ $m_\perp^{ext} = m_/^{ext} = 0.24$ $m_\parallel^{int} = 0.17$ $m_\perp^{int} = m_/^{int} = 0.019$	data from [65]
3D atria	Courtemanche, bidomain	same as ventricles but rescaled by a factor 1.05	corresponding to a longitudinal velocity 0.5 m/s [5, 6]

Table 2: Monodomain and bidomain electrical conductivities of the various cardiac components, as defined in section 3.2.
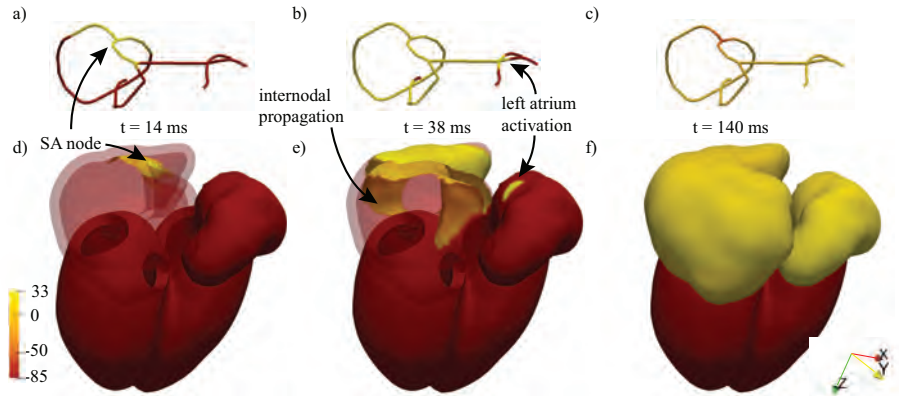

Figure 17: Atrial depolarization. Transmembrane potential in the fast conduction atrial bundles at a) $t = 14$ ms b) $t = 38$ ms and c) $t = 140$ ms, whereas the corresponding depolarization of the 3D myocardium is shown in d), e) and f), respectively. In (a,d) the depolarization front has just been initiated in the SA–node, in (b,e) most of 3D right atrium is depolarized and the depolarization front just reached the left atrium through the 1D bundles. In c) both atria are depolarized and the right one starts the repolarize.

(panels a,b,c) and of the 3D atrial myocardium (panels d,e,f) at three differ-
ent time instants, with t defined as the time lag with respect to the SA–node
activation (corresponding to $t = 0$). In both 1D and 3D media, the trans-
membrane potential, v, has an initial resting value of -80 mV (red isolevel)
and transiently reaches a positive value (yellow isolevel) as the depolarization
front advances. The latter originates at the SA–node, where the effect of the
pace–maker cells translates into an initial electrical stimulus (4) activating the
SA–node (Figure 17 a), which then advances simultaneously into the three in-
ternodal pathways, namely the Thorel's posterior internodal tract, the Wencke-
bach's bundle-middle internodal tract and the anterior internodal tract that
further bifurcates in the Bachmann's bundle towards the left atrium (Figure 17
b). The propagation fronts in these three internodal pathways then recollect
at the bottom of the atrial network into the AV–node (see Figure 17 b) after
about 25-40 ms from the SA–node activation, first throughout the anterior and
middle bundle and later throughout the posterior one. In the meantime the
depolarization front propagates in the 1D network of bundles, it activates the
surrounding atrial myocardium through the CNs, thus triggering another depo-
larization front in the 3D media, as shown by the incipient myocardial activation
near by the SA–node in Figure 17(d). Although the conduction speed in the
3D myocardium is anisotropic and the transmembrane depolarization advances
faster in the directions aligned with the muscular fibers (owing to a larger elec-
trical conductivity), the myocardium depolarization is about three times slower
than the one in the bundles. This leads to a complete activation of both 3D
atrial chambers after about 140 ms, as visible in Figure 17 (f). Interestingly,
the endocardial and epicardial depolarization fronts in Figure 17 (e), reveal that
the epicardium depolarizes with few milliseconds delay with respect to the en-
docadium, which corresponds to the time lag needed by the 3D depolarization
front (originated at the bundles placed within the endocardium) to propagate
across the atrial wall in the cross–fiber directions.

In non–pathological profiles, as is the case here, the signal carried into the
AV–node by the internodal pathways propagates from the left atrium to the ven-
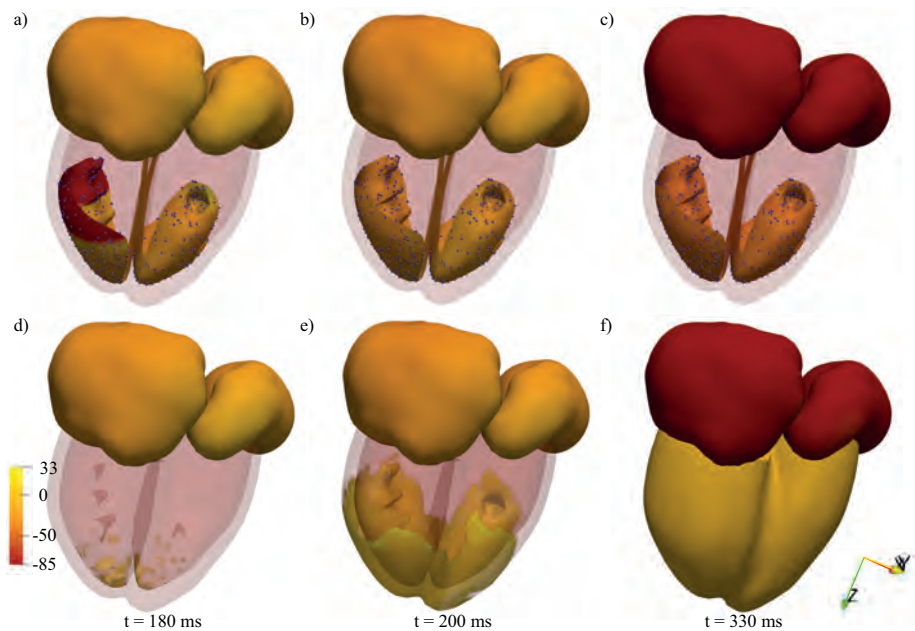
31

Figure 18: Ventricular depolarization. Transmembrane potential at a) $t = 180$ ms b) $t = 200$ ms and c) $t = 330$ ms showing the action potential propagation front in the Purkinje and the locations of the PMJs coupling the Purkinje with the ventricular myocardium. The same data are reported in panels d) e) and f) but using a different transparency so to better visualize the 3D ventricular depolarization. In panels (a,b) both atria have been activated, whereas in panel (c) they are completely depolarized.

tricles only through the AV–node itself. In the AV–node, the propagation speed of the depolarization front greatly reduces, yielding a delay of about 100 ms between the atrial and the subsequent ventricular depolarization (Figure 18 a). After the depolarization front swept the AV–node, it reaches the bundle of His before propagating in the two ventricular chambers through left bundle and right bundles (Figure 18 a), which, in turn, are electrically connected to the Purkinje network. The latter carry the depolarization front in both ventricular chambers with a propagation speed of about 4 m/s (roughly ten times the surrounding myocardial tissue), first activating the lower part of the ventricle (Figure 18 d,e) and then the upper part (Figure 18 e,f). As visible in the same panels, the activation of the 2D Purkinje network precedes the surrounding 3D

32

ventricular activation, thus yielding a more synchronous depolarization of the 3D media. As visible in the upper panels of Figure 18, the 3D myocardium is

560 electrically activated by the 2D Purkinje network through the PMJs with an orthodromic delay of 5 ms. Importantly, when the ventricles are almost completely depolarized, the atria are repolarizing (Figure 18 e) and, successively, when the ventricles are completely activated, the atria are fully repolarized (Figure 18 f).
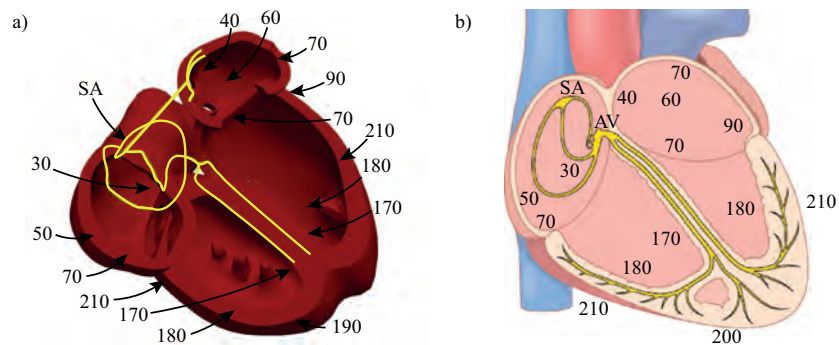

Figure 19: Time lag (in ms) of the cardiac depolarization at various heart locations with respect the SA–node stimulus according to a) our numerical model and b) medical atlas [5].

565 Figure 19 compares the electrical activation at various cardiac locations reported in medical atlas [5] with respect to those obtained by our computational model, where each number corresponds to the time interval in milliseconds that lapse between the activation of SA–node and that of the location indicated by the number: an overall good agreement can be observed. In particular, the fast

570 atrial 1D conduction system (internodal pathways) correctly ensures the activation of the atrioventricular node after 30 milliseconds from the activation of the SA–node, with a perfect match with what observed in–vivo reality. Furthermore, the slower conduction velocity in the AV–node and the subsequent rapid spreading of the depolarization front in the 2D Purkinje network provide the

575 correct activation of the entire ventricular endocardium, including the papillary muscles.

a)

right
bundle block

left
bundle block

b)

septal

appendage

left
ventricle
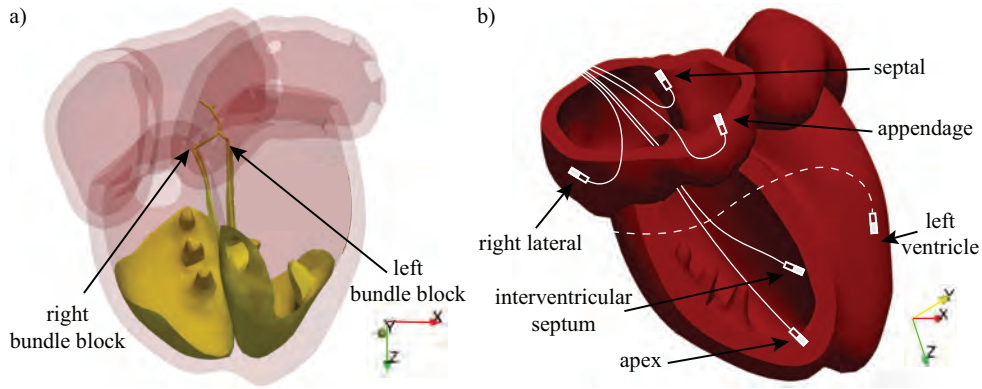
right lateral

interventricular
septum

apex

Figure 20: a) Positions of the right and left ventricular bundle blocks. b) Most common leads potitioning for atrial and ventricular pacemaking [81].

5.2. Pathologic and aided electrophysiology: bundle branch block and artificial pacing

The present high–fidelity computational framework for the whole heart electrophysiology allows also to model cardiac pathologies and predict the effect of medical devices, such as the artificial pacing applied to a patient affected by a bundle branch block. The latter consists of the delay or blockage of the electrical propagation within a ventricular bundle (see Figure 20a), thus implying a delayed activation of some areas of the ventricular myocardium and a consequent anomaly in the activation/contraction profile of the ventricle [82, 83]. Possible causes originating a bundle branch block include heart attacks (myocardial infarction involving the bundles), myocarditis (viral/bacterial infection of the heart muscle), cardiomyopathy (thickened/stiffened or weakened heart muscle), congenital heart abnormality (such as atrial septal defect) or even high blood pressure (hypertension) [84, 85].

The occurrence of this pathology is included in the 1D fast conductivity bundles and in the 2D Purkinje network as a local reduction of the electrical conductivities proportionally to the severity of the bundle branch delay, whereas a null conductivity tensor is used to simulate a complete block of the bundle. The resulting pathologic activation in the case of a right bundle branch block

34

is reported in Figure 21 showing that, despite the depolarization of the left ventricular myocardium is correctly initiated after about 180 ms (panel 21a), the missing propagation of the depolarization front through the right Purkinje network prevents the normal depolarization of the ventricular myocardium observed in the healthy cases (Figure 18 d,e). However, as the left and right ventricular myocardium are a unique 3D excitable media, the right ventricular depolarization is triggered by the surrounding left ventricular one with a delay of about 20 ms and the propagation front then travels throughout the chambers (panel 21b). Nevertheless, as the conduction speed in the 3D myocardium is about ten times slower than the one in the Purkinje network, the depolarization of the right chamber results significantly delayed with respect to healthy conditions with an asynchronous depolarization of the apical, equatorial and basal myocytes (Figure 21c), which would entail an inefficient systolic contraction [5]. Vice–versa, the presence of a left bundle block, shown in Figure 22, yields a delayed activation of the left ventricle owing to the missing propagation in the left ventricular bundle and Purkinje network.
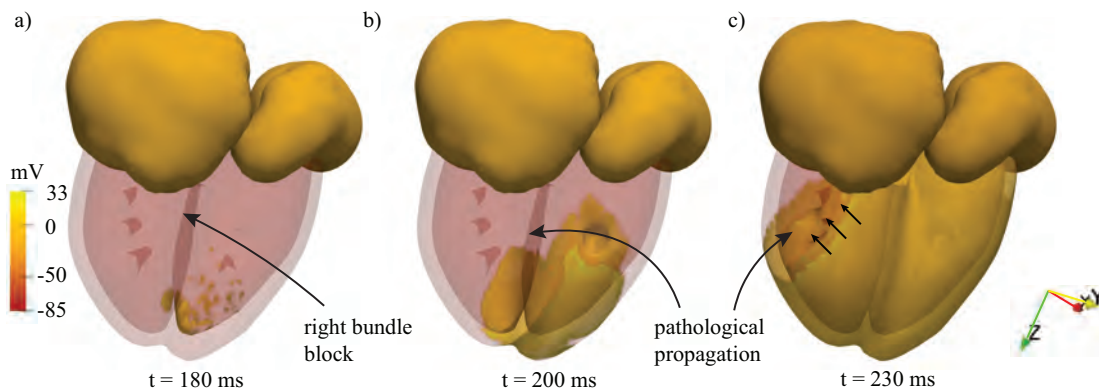

Figure 21: Pathologic ventricular activation in the case of right bundle block at various time instants with respect the SA–node activation. In particular, the time instants of panels (a) and (b) corresponds to the ones for the healthy cases reported in Figure 18. The black arrow in panel c) highlights the delayed right ventricle depolarization caused by the disease.

Bundle block pathologies, as well as other cardiac diseases such as sinus node
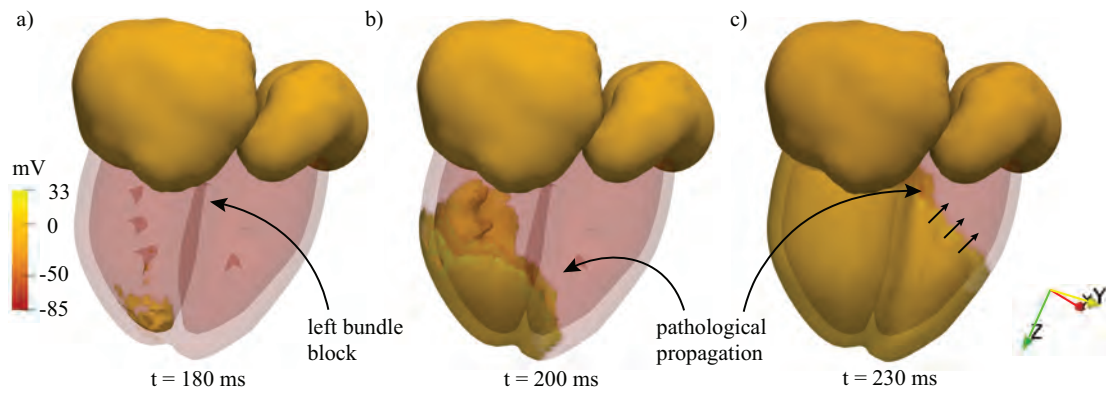
Figure 22: Pathologic ventricular activation in the case of left bundle block at various time instants with respect the SA–node activation. In particular, the time instants of panels (a) and (b) correspond to the ones for the healthy cases reported in Figure 18. The black arrow in panel c) highlights the delayed left ventricle depolarization caused by the disease.
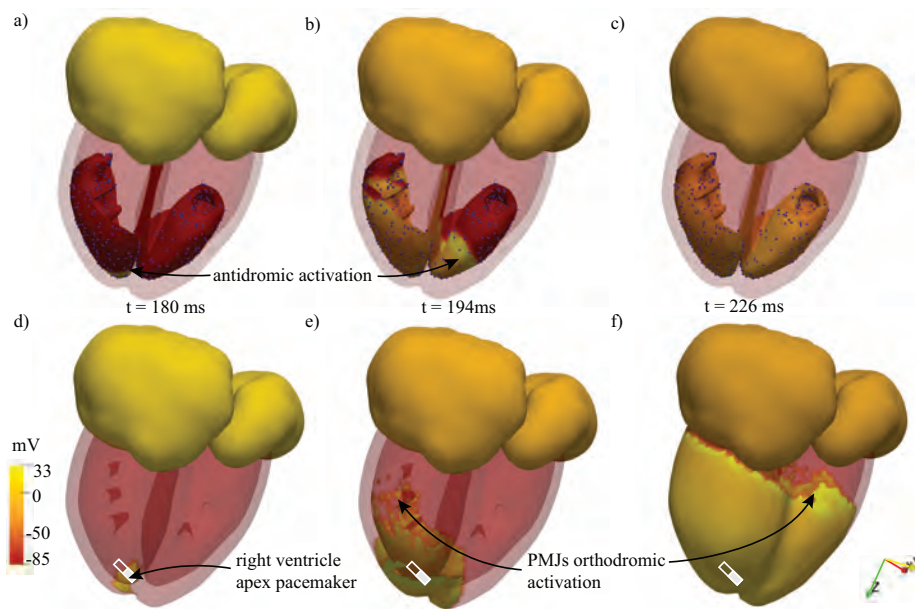

Figure 23: Cardiac electrophysiology with an artificial pacing at the ventricular apex, the white symbol indicates the lead location. Panels (a,b,c) show the action potential front in the Purkinje network while panels (d,e,f) describe corresponding depolarization of the surrounding 3D myocardium. The AV–node communication is interrupted (AV block).
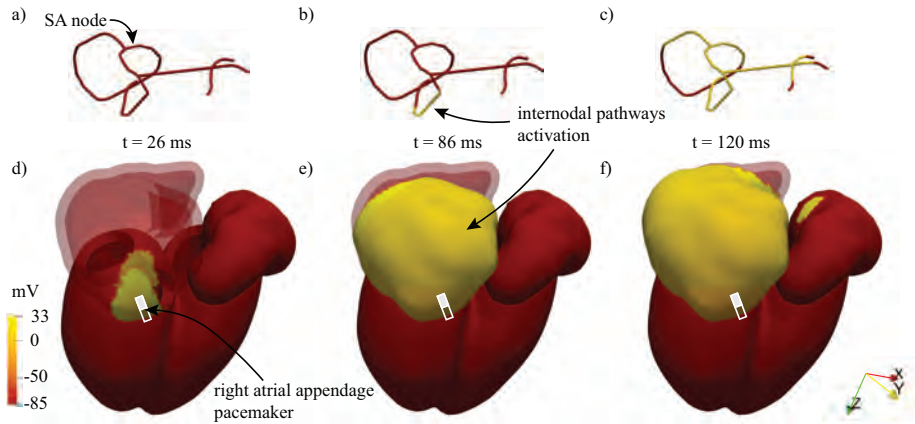
Figure 24: Cardiac electrophysiology with an artificial pacing at the atrial appendage, the white symbol indicates the lead location. Panels (a,b,c) show the action potential depolarization front within the internodal pathways, whereas panels (d,e,f) indicate the corresponding 3D myocardium.

dysfunction and intermittent AV block [86, 87] are often treated with artificial stimulation through the implantation of an artificial cardiac pacemaker [81], which consists of inserting an artificial lead in contact with the internal muscular wall (endocardium) inducing the periodic depolarization of the surrounding tissue. The effect of an implanted pacemaker lead can be accounted for in the model through an additional stimulation current I^s in equation (1) acting on the 3D myocardium and localized at the lead position. Among the most common atrial (septal, right lateral, appendage) and ventricular (apex, interventricular septum, left ventricle) leads implantation sites reported in Figure 20(b), here we consider a ventricular apex pacing to mitigate a pathologic atrioventricular block (inability of the signal to cross the AV–node) simulated by setting the conductivity of the AV–node to zero. As shown in Figure 23(a), although the ventricular myocardium is not activated by the fast conduction Purkinje complex, as in healthy conditions, the pacing lead implanted within the apical tissue of the right ventricle induces an electrical stimulus with a delay of 160 seconds with respect to the SA–node. In particular, the depolarization front propa-

37

gates from the 3D myocardium activated by the lead to the Purkinje network through the PMJs (with an antidromic delay of 3 ms, see Figure 23 b,e), and then rapidly propagates through the rest of the Purkinje network which, in turn, triggers the depolarization of the underlying 3D myocardial tissue through the downstream PMJs (with an orthodromic communication delay, see Figure 23 e). Hence, in agreement with the medical evidence, the presence of an artificial stimulation through an implanted lead manages to activate the Purkinje network downstream the bundle block and to recover an effective depolarization of the ventricular myocardium in a similar fashion as the healthy depolarization pattern studied above and reported in Figure 18.

In addition, Figure 24 shows the cardiac electrophysiology corresponding to an atrial pacemaking, where the lead is positioned in the right atrial appendage [88], one of the most frequent implantation sites for an atrial lead [81]. Initially, the electrical stimulus provided by the lead only depolarizes a surrounding piece of the 3D atrial myocardium (panel 24 d), whereas the atrial 1D bundles are not directly activated by the lead (panel 24 a). The electrical depolarization front propagates in the 3D myocardium until reaching and, consequently, activating the fast conduction bundles (see panel 24 b), which then rapidly propagates the depolarization front in the whole 1D network, including the left atrial network (panel 24 c). The combined effect of slow (3D) and fast (1D) depolarization fronts induced by the atrial lead thus yields a homogeneous activation of the left atrium. Nevertheless, compared to healthy propagation shown in Figure 17 b), the atrial depolarization occurs with a delay of approximately 95 ms.

6. Discussion

In this work, a numerical framework for solving the cardiac electrophysiology of the whole human heart in healthy and pathologic conditions has been proposed. According to the complex spatial distribution of the electrophysiology properties of the heart, the whole cardiac geometry is decomposed into a set of coupled conductive media of different topology, namely (i) a 1D network

38

of bundles comprising a fast conduction atrial network, the AV–node and the ventricular bundles; (ii) a 2D Purkinje network; and (iii) the 3D atrial and ventricular myocardium. These overlapping subdomains are two–way electrically coupled and the advancing depolarization front can propagate from one media to another, as happens in physiological conditions. Specifically, in a healthy heart, the fast conduction atrial network activates the 3D atrial myocardium and the AV–node which, in turn, activates the ventricular bundles transmitting the depolarization front to the Purkinje network which rapidly activates the 3D ventricular myocardium through the PMJs. Nevertheless, different activation patterns, also including backward activation from the 3D myocardium to the bundles and/or to the Purkinje, may occur in pathological conditions as observed in section 5.2. Although the propagation of the depolarization front in all these conductive media is governed by the bidomain/monodomain equations, the heterogeneity of the cardiac electrophysiology properties at the cellular scale corresponds to different electrical conductivities and ionic currents across the myocytes membrane at the continuum scale, which has been accounted in the numerical model through non–uniform conductivity tensors which depend on the local fiber orientation and using three different cell models. Specifically, the Courtemanche cell model [1] is used for the atrial myocytes (and the corresponding internodal pathways), the Stewart cell model [2] is adopted for the Purkinje Network, whereas the transmembrane ionic fluxes in the ventricular myocytes are solved through the ten Tusscher–Panfilov cell model [3], which correctly reproduces the action potential within ventricular myocytes. These models are coupled with the bidomain/monodomain equations, which are discretized in space using an in–house finite–volume method tailored for 1D, 2D and 3D complex geometries and the explicit Rush–Larsen temporal integration scheme guarantees enhanced stability properties. The numerical solver has been thoroughly validated with available benchmark results from the literature [65, 78] and the resulting depolarization within the whole heart well agrees with in–vivo observations [5].

The whole solver is GPU–accelerated using CUDA Fortran with the exten-

39

sive use of kernel loop directives (CUF kernels) providing an unprecedented speedup, thus allowing to solve a complete heartbeat in less than 8 wall–clock hours using Tesla V100 GPU devices. It should be noted that such computational cost could be further reduced either resorting to a monodomain model for the 3D myocardium corresponding to a 1.5 wall–clock hours per heartbeat, or using the next generation Tesla A100 GPU devices which are expected to provide a further acceleration of about four times while keeping the same code [89].

Stimulus properties
SA size
SA orientation

Internodal pathways
control points position
pathways conductivity
size of connections

Volume
right atrial volume
left atrial volume
ventricles volume

Cellular models
Courtemanche model
AV node properties
Stewart cellular model
ten Tusscher model

Fiber orientation
atrial fiber orientation
ventricular fiber orientation

Conductivities
atrial conductivity
AV conductivity
Purkinje conductivity
ventricular conductivity

Purkinje network
PMJs distribution
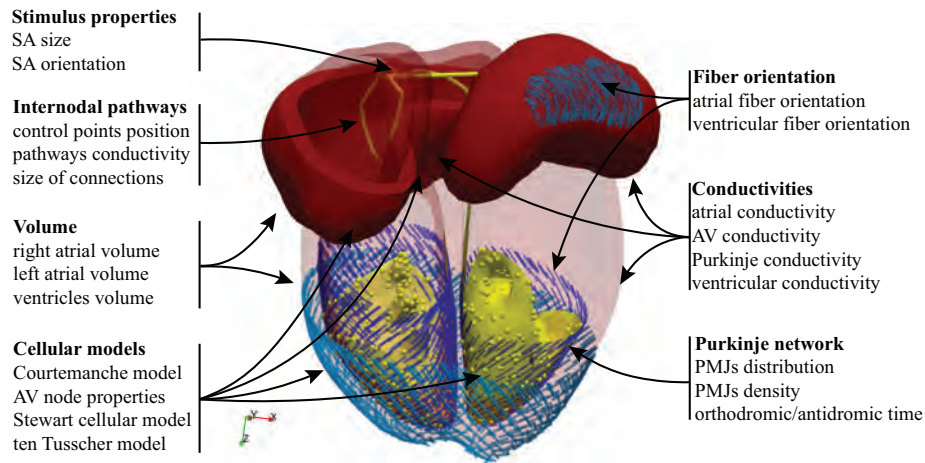PMJs density
orthodromic/antidromic time

Figure 25: Summary of the electrophysiology components having a high variability among individuals and which may be studied systematically with the proposed numerical model through an UQ analysis.

The resulting digital twin of the human cardiac electrophysiology could be applied to study spatiotemporal alternans patterns within ventricles and assess the role of the Purkinje network in the initiation/suppression of arrhythmia, also through the use of appropriate spatiotemporal correlation indices [90]. A natural development of the model is the integration of the corresponding electrocardiogram profile (ECG) either using a pseudo-ECG formulation [91] or a more realistic torso model with a detailed body surface potential analysis [92]. The latter would allow not only to directly compute the ECG problems of a given cardiac configuration, but also to determine in a reverse fashion the elec-

40

trophysiology network corresponding to an observed pathological ECG [93].

Importantly, the computational high–performance of the solver and its versatility in controlling the geometrical and electrical properties of the whole cardiac electrophysiology open the way for systematic uncertainty quantification (UQ) analyses. The human electrophysiology system, indeed, presents high variability in the several of its components such as the fiber orientations, conductivity tensors, chambers volume, internodal pathways positions and the density of PMJs, and our numerical framework is designed to easily control and vary all these relevant quantities summarized in Figure 25. The splitting of the cardiac electrophysiology system in a set of interconnected conductive media not only reduces the computational cost, but also provides an ideal framework for investigating the effect of an electrical or geometrical modification of the fast conduction network (bundles and/or Purkinje) on the cardiac depolarization, thus allowing to optimize cardiac resynchronization therapies or invasive surgical procedures [94, 95, 96]. Furthermore, the computational bottleneck given by the 3D bidomain simulations can be circumvented by exploiting appropriate multi–fidelity strategies [97, 98, 99]. On the other hand, a monodomain inverse conductivity problem (MICP) [100, 101] can be solved for the fast conduction network of bundles to calibrate the electrical conductivities of monodomain model in order to match medical data acquired in–vivo. As a last comment, the relationship between the cardiac valves functioning [102, 103, 9] and the geometry of the Purkinje network, papillary muscles and chordae tendinae could be investigated by integrating our electrophysiology model within a fluid–structure solver [41], so to also account for the cardiac hemodynamics and tissues kinematics in the UQ analysis.

Acknowledgements

References

[1] M. Courtemanche, R. J. Ramirez, S. Nattel, Ionic mechanisms underlying human atrial action potential properties: insights from a mathematical model, American Journal of Physiology-Heart and Circulatory Physiology 275 (1) (1998) H301–H321.

[2] P. Stewart, O. V. Aslanidi, D. Noble, P. J. Noble, M. R. Boyett, H. Zhang, Mathematical models of the electrical action potential of purkinje fibre cells, Philosophical Transactions of the Royal Society A: Mathematical, Physical and Engineering Sciences 367 (1896) (2009) 2225–2255.

[3] K. Ten Tusscher, A. Panfilov, Cell model for efficient simulation of wave propagation in human ventricular tissue under normal and pathological conditions, Physics in Medicine & Biology 51 (23) (2006) 6141.

[4] A. Kaboudian, E. M. Cherry, F. H. Fenton, Real-time interactive simulations of large-scale systems on personal computers and cell phones: Toward patient-specific heart modeling and other applications, Science advances 5 (3) (2019) eaav6019.

[5] J. E. Hall, Guyton and Hall textbook of medical physiology e-Book, Elsevier Health Sciences, 2015.

[6] D. M. Harrild, C. S. Henriquez, A computer model of normal conduction in the human atria, Circulation research 87 (7) (2000) e25–e36.

[7] T. N. James, The internodal pathways of the human heart, Progress in cardiovascular diseases 43 (6) (2001) 495–535.

[8] F. Pashakhanloo, D. A. Herzka, H. Ashikaga, S. Mori, N. Gai, D. A. Bluemke, N. A. Trayanova, E. R. McVeigh, Myofiber architecture of the human atria as revealed by submillimeter diffusion tensor imaging, Circulation: arrhythmia and electrophysiology 9 (4) (2016) e004133.

[9] S. Karas Jr, R. C. Elkins, Mechanism of function of the mitral valve leaflets, chordae tendineae and left ventricular papillary muscles in dogs, Circulation research 26 (6) (1970) 689–696.

[10] R. Bordas, V. Grau, R. Burton, P. Hales, J. Schneider, D. Gavaghan, P. Kohl, B. Rodriguez, Integrated approach for the study of anatomical variability in the cardiac purkinje system: from high resolution mri to electrophysiology simulation, in: 2010 Annual International Conference of the IEEE Engineering in Medicine and Biology, IEEE, 2010, pp. 6793–6796.

[11] A. Saha, S. Roy, Papillary muscles of right ventricle - morphological variations and its clinical relevance, Cardiovascular Pathology 34 (2018) 22–27.

[12] R. A. Bergman, A. K. Afifi, et al., Atlas of microscopic anatomy.

[13] J. Tranum-Jensen, A. Wilde, J. T. Vermeulen, M. J. Janse, Morphology of electrophysiologically identified junctions between purkinje fibers and ventricular muscle in rabbit and pig hearts., Circulation research 69 (2) (1991) 429–437.

[14] O. Berenfeld, J. Jalife, Purkinje-muscle reentry as a mechanism of polymorphic ventricular arrhythmias in a 3-dimensional model of the ventricles, Circulation Research 82 (10) (1998) 1063–1077.

[15] G. A. Holzapfel, R. W. Ogden, Constitutive modelling of passive myocardium: a structurally based framework for material characterization, Philosophical Transactions of the Royal Society A: Mathematical, Physical and Engineering Sciences 367 (1902) (2009) 3445–3475.

[16] G. Seemann, C. Höper, F. B. Sachse, O. Dössel, A. V. Holden, H. Zhang, Heterogeneous three-dimensional anatomical and electrophysiological model of human atria, Philosophical Transactions of the Royal Society A: Mathematical, Physical and Engineering Sciences 364 (1843) (2006) 1465–1481.

[17] D. Nickerson, N. Smith, P. Hunter, New developments in a strongly cou-
pled cardiac electromechanical model, EP Europace 7 (s2) (2005) S118–
S127.

[18] S. G. Campbell, E. Howard, J. Aguado-Sierra, B. A. Coppola, J. H.
Omens, L. J. Mulligan, A. D. McCulloch, R. C. Kerckhoffs, Effect of
transmurally heterogeneous myocyte excitation–contraction coupling on
canine left ventricular electromechanics, Experimental physiology 94 (5)
(2009) 541–552.

[19] G. Buckberg, A. Mahajan, S. Saleh, J. I. Hoffman, C. Coghlan, Structure
and function relationships of the helical ventricular myocardial band, The
Journal of thoracic and cardiovascular surgery 136 (3) (2008) 578–589.

[20] R. Doste, D. Soto-Iglesias, G. Bernardino, A. Alcaine, R. Sebastian,
S. Giffard-Roisin, M. Sermesant, A. Berruezo, D. Sanchez-Quintana,
O. Camara, A rule-based method to model myocardial fiber orientation in
cardiac biventricular geometries with outflow tracts, International journal
for numerical methods in biomedical engineering 35 (4) (2019) e3185.

[21] N. A. Trayanova, Whole-heart modeling: applications to cardiac elec-
trophysiology and electromechanics, Circulation research 108 (1) (2011)
113–128.

[22] A. J. Pullan, K. A. Tomlinson, P. J. Hunter, A finite element method for
an eikonal equation model of myocardial excitation wavefront propagation,
SIAM Journal on Applied Mathematics 63 (1) (2002) 324–350.

[23] J. J. B. Jack, D. Noble, R. W. Tsien, Electric current flow in excitable
cells, Clarendon Press Oxford, 1975.

[24] L. Leon, F. Roberge, Directional characteristics of action potential prop-
agation in cardiac muscle. a model study., Circulation research 69 (2)
(1991) 378–395.

44

[25] A. Bueno-Orovio, D. Kay, V. Grau, B. Rodriguez, K. Burrage, Fractional diffusion models of cardiac electrical propagation: role of structural heterogeneity in dispersion of repolarization, Journal of the Royal Society Interface 11 (97) (2014) 20140352.

[26] D. E. Hurtado, S. Castro, A. Gizzi, Computational modeling of non-linear diffusion in cardiac electrophysiology: A novel porous-medium approach, Computer Methods in Applied Mechanics and Engineering 300 (2016) 70–83.

[27] N. G. Sepulveda, B. J. Roth, J. P. Wikswo Jr, Current injection into a two-dimensional anisotropic bidomain., Biophysical journal 55 (5) (1989) 987.

[28] L. Tung, A bi-domain model for describing ischemic myocardial dc potentials., Ph.D. thesis, Massachusetts Institute of Technology (1978).

[29] J. Sundnes, G. T. Lines, X. Cai, B. F. Nielsen, K.-A. Mardal, A. Tveito, Computing the electrical activity in the heart, Vol. 1, Springer Science & Business Media, 2007.

[30] E. Vigmond, R. W. Dos Santos, A. Prassl, M. Deo, G. Plank, Solvers for the cardiac bidomain equations, Progress in biophysics and molecular biology 96 (1-3) (2008) 3–18.

[31] J. P. Wikswo Jr, S.-F. Lin, R. A. Abbas, Virtual electrodes in cardiac tissue: a common mechanism for anodal and cathodal stimulation, Biophysical journal 69 (6) (1995) 2195–2210.

[32] A. Muzikant, C. Henriquez, Validation of three-dimensional conduction models using experimental mapping: are we getting closer?, Progress in biophysics and molecular biology 69 (2-3) (1998) 205–223.

[33] B. J. Roth, Meandering of spiral waves in anisotropic cardiac tissue, Physica D: Nonlinear Phenomena 150 (1-2) (2001) 127–136.

[34] N. Trayanova, Defibrillation of the heart: insights into mechanisms from modelling studies, Experimental physiology 91 (2) (2006) 323–337.

[35] M. Potse, B. Dubé, J. Richer, A. Vinet, R. M. Gulrajani, A comparison of monodomain and bidomain reaction-diffusion models for action potential propagation in the human heart, IEEE Transactions on Biomedical Engineering 53 (12) (2006) 2425–2435.

[36] M. Wilhelms, H. Hettmann, M. M. C. Maleckar, J. T. Koivumäki, O. Dössel, G. Seemann, Benchmarking electrophysiological models of human atrial myocytes, Frontiers in physiology 3 (2013) 487.

[37] S. Inada, J. Hancox, H. Zhang, M. Boyett, One-dimensional mathematical model of the atrioventricular node including atrio-nodal, nodal, and nodal-his cells, Biophysical journal 97 (8) (2009) 2117–2127.

[38] V. D. Corino, F. Sandberg, L. T. Mainardi, L. Sornmo, An atrioventricular node model for analysis of the ventricular response during atrial fibrillation, IEEE transactions on biomedical engineering 58 (12) (2011) 3386–3395.

[39] B. Baillargeon, N. Rebelo, D. D. Fox, R. L. Taylor, E. Kuhl, The living heart project: a robust and integrative simulator for human heart function, European Journal of Mechanics-A/Solids 48 (2014) 38–47.

[40] S. Sugiura, T. Washio, A. Hatano, J. Okada, H. Watanabe, T. Hisada, Multi-scale simulations of cardiac electrophysiology and mechanics using the university of tokyo heart simulator, Progress in biophysics and molecular biology 110 (2-3) (2012) 380–389.

[41] F. Viola, V. Meschini, R. Verzicco, Fluid–structure-electrophysiology interaction (fsei) in the left-heart: A multi-way coupled computational model, European Journal of Mechanics-B/Fluids 79 (2020) 212–232.

[42] E. J. Vigmond, C. Clements, Construction of a computer model to in-vestigate sawtooth effects in the purkinje system, IEEE transactions on biomedical engineering 54 (3) (2007) 389–399.

[43] T. Lassila, M. Lange, A. R. P. Perez, K. Lekadir, X. Albà, G. Piella, A. F. Frangi, Electrophysiology model for a human heart with ischemic scar and realistic purkinje network, in: Statistical Atlases and Computational Models of the Heart, Springer, 2015, pp. 90–97.

[44] M. Deo, P. Boyle, G. Plank, E. Vigmond, Arrhythmogenic mechanisms of the purkinje system during electric shocks: a modeling study, Heart rhythm 6 (12) (2009) 1782–1789.

[45] M. Deo, P. M. Boyle, A. M. Kim, E. J. Vigmond, Arrhythmogenesis by single ectopic beats originating in the purkinje system, American Journal of Physiology-Heart and Circulatory Physiology 299 (4) (2010) H1002–H1011.

[46] E. Behradfar, A. Nygren, E. J. Vigmond, The role of purkinje-myocardial coupling during ventricular arrhythmia: a modeling study, PloS one 9 (2).

[47] T. Ijiri, T. Ashihara, T. Yamaguchi, K. Takayama, T. Igarashi, T. Shimada, T. Namba, R. Haraguchi, K. Nakazawa, A procedural method for modeling the purkinje fibers of the heart, The journal of physiological sciences (2008) 0810170079–0810170079.

[48] A. Lopez-Perez, R. Sebastian, J. M. Ferrero, Three-dimensional cardiac computational modelling: methods, features and applications, Biomedical engineering online 14 (1) (2015) 35.

[49] C. Vergara, M. Lange, S. Palamara, T. Lassila, A. F. Frangi, A. Quarteroni, A coupled 3d–1d numerical monodomain solver for cardiac electrical activation in the myocardium with detailed purkinje network, Journal of Computational Physics 308 (2016) 218–238.

47

[50] P. Pathmanathan, M. O. Bernabeu, R. Bordas, J. Cooper, A. Garny, J. M. Pitt-Francis, J. P. Whiteley, D. J. Gavaghan, A numerical guide to the solution of the bidomain equations of cardiac electrophysiology, Progress in biophysics and molecular biology 102 (2) (2010) 136–155.

[51] N. A. Trayanova, J. Constantino, V. Gurev, Electromechanical models of the ventricles, American Journal of Physiology-Heart and Circulatory Physiology 301 (2) (2011) H279–H286.

[52] J. Cooper, A. Corrias, D. Gavaghan, D. Noble, Considerations for the use of cellular electrophysiology models within cardiac tissue simulations, Progress in biophysics and molecular biology 107 (1) (2011) 74–80.

[53] A. Loppini, A. Gizzi, R. Ruiz-Baier, C. Cherubini, F. H. Fenton, S. Filippi, Competing mechanisms of stress-assisted diffusivity and stretch-activated currents in cardiac electromechanics, Frontiers in physiology 9 (2018) 1714.

[54] R. H. Clayton, Y. Aboelkassem, C. D. Cantwell, C. Corrado, T. Delhaas, W. Huberts, C. L. Lei, H. Ni, A. V. Panfilov, C. Roney, et al., An audit of uncertainty in multi-scale cardiac electrophysiology models, Philosophical Transactions of the Royal Society A 378 (2173) (2020) 20190335.

[55] E. C. Vasconcellos, E. W. Clua, F. H. Fenton, M. Zamith, Accelerating simulations of cardiac electrical dynamics through a multi-gpu platform and an optimized data structure, Concurrency and Computation: Practice and Experience 32 (5) (2020) e5528.

[56] E. Koprla, L. Nemeseri, Essential features of endocardial and myocardial morphology: Sem and tem studies., Acta Physiologica Hungarica 64 (1) (1984) 65–79.

[57] G. M. Hutchins, B. H. Bulkley, G. W. Moore, M. A. Piasio, F. T. Lohr, Shape of the human cardiac ventricles, The American journal of cardiology 41 (4) (1978) 646–654.

48

[58] A. Ansari, S. Yen Ho, R. H. Anderson, Distribution of the purkinje fibres in the sheep heart, The Anatomical Record: An Official Publication of the American Association of Anatomists 254 (1) (1999) 92–97.

[59] T. Shimada, Purkinje fibers of the heart, Shinyaku to Chiryou 42 (1992) 11–13.

[60] C. Vergara, S. Palamara, D. Catanzariti, F. Nobile, E. Faggiano, C. Pangrazzi, M. Centonze, M. Maines, A. Quarteroni, G. Vergara, Patient-specific generation of the purkinje network driven by clinical measurements of a normal propagation, Medical & biological engineering & computing 52 (10) (2014) 813–826.

[61] A. Saha, S. Roy, Papillary muscles of left ventricle - morphological variations and its clinical relevance, Indian heart journal 70 (6) (2018) 894–900.

[62] G. Nigri, L. Di Dio, C. Baptista, Papillary muscles and tendinous cords of the right ventricle of the human heart morphological characteristics, Surgical and Radiologic Anatomy 23 (1) (2001) 45–49.

[63] G. D. Buckberg, Basic science review: the helix and the heart, The Journal of Thoracic and Cardiovascular Surgery 124 (5) (2002) 863–883.

[64] R. Greenbaum, S. Y. Ho, D. Gibson, A. Becker, R. Anderson, Left ventricular fibre architecture in man., Heart 45 (3) (1981) 248–263.

[65] S. A. Niederer, E. Kerfoot, A. P. Benson, M. O. Bernabeu, O. Bernus, C. Bradley, E. M. Cherry, R. Clayton, F. H. Fenton, A. Garny, et al., Verification of cardiac tissue electrophysiology simulators using an n-version benchmark, Philosophical Transactions of the Royal Society A: Mathematical, Physical and Engineering Sciences 369 (1954) (2011) 4331–4351.

[66] G. Del Corso, R. Verzicco, F. Viola, On the electrophysiology of the atrial fast conduction system: model validation and uq analysis, Acta Mechanica Sinica (2021) 1.

49

[67] F. Moukalled, L. Mangani, M. Darwish, The finite volume method in computational fluid dynamics, Vol. 113, Springer, 2016.

[68] S. Rush, H. Larsen, A practical algorithm for solving dynamic membrane equations, IEEE Transactions on Biomedical Engineering (4) (1978) 389–392.

[69] M. E. Marsh, S. T. Ziaratgahi, R. J. Spiteri, The secrets to the success of the rush–larsen method and its generalizations, IEEE transactions on biomedical engineering 59 (9) (2012) 2506–2515.

[70] L. N. Trefethen, D. Bau III, Numerical linear algebra, Vol. 50, Siam, 1997.

[71] G. Ruetsch, M. Fatica, CUDA Fortran for scientists and engineers: best practices for efficient CUDA Fortran programming, Elsevier, 2013.

[72] R. H. Anderson, S. Mori, D. E. Spicer, D. Sanchez-Quintana, B. Jensen, The anatomy, development, and evolution of the atrioventricular conduction axis, Journal of cardiovascular development and disease 5.

[73] N. Ono, T. Yamaguchi, H. Ishikawa, M. Arakawa, N. Takahashi, T. Saikawa, T. Shimada, Morphological varieties of the purkinje fiber network in mammalian hearts, as revealed by light and electron microscopy, Archives of histology and cytology 72 (3) (2009) 139–149.

[74] B. R. Liu, E. M. Cherry, Image-based structural modeling of the cardiac purkinje network, BioMed research international 2015.

[75] S. Tawara, Das Reizleitungssystem des Säugetierherzens: eine anatomisch-histologische Studie über das Atrioventrikularbündel und die Purkin-jeschen Fäden, Fischer, 1906.

[76] O. S. Narula, Sinus node re-entry: a mechanism for supraventricular tachy-cardia, Circulation 50 (6) (1974) 1114–1128.

[77] S. Niederer, L. Mitchell, N. Smith, G. Plank, Simulating human cardiac electrophysiology on clinical time-scales, Frontiers in physiology 2 (2011) 14.

[78] G. Cuccuru, G. Fotia, F. Maggio, J. Southern, Simulating cardiac electrophysiology using unstructured all-hexahedra spectral elements, BioMed research international 2015.

[79] M. Perego, A. Veneziani, An efficient generalization of the rush-larsen method for solving electro-physiology membrane equations, Electronic Transactions on Numerical Analysis 35 (2009) 234–256.

[80] O. Dössel, M. W. Krueger, F. M. Weber, M. Wilhelms, G. Seemann, Computational modeling of the human atrial anatomy and electrophysiology, Medical & biological engineering & computing 50 (8) (2012) 773–799.

[81] S. Pakarinen, L. Toivonen, Minimizing ventricular pacing by a novel atrioventricular (av) delay hysteresis algorithm in patients with intact or compromised intrinsic av conduction and different atrial and ventricular lead locations, Annals of medicine 45 (5-6) (2013) 438–445.

[82] A. Takeshita, L. L. Basta, J. M. Kioschos, Effect of intermittent left bundle branch block on left ventricular performance, The American journal of medicine 56 (2) (1974) 251–255.

[83] H. Xiao, C. Lee, D. Gibson, Effect of left bundle branch block on diastolic function in dilated cardiomyopathy., Heart 66 (6) (1991) 443–447.

[84] H. Mahrholdt, A. Wagner, C. C. Deluigi, E. Kispert, S. Hager, G. Meinhardt, H. Vogelsberg, P. Fritz, J. Dippon, C.-T. Bock, et al., Clinical perspective, Circulation 114 (15) (2006) 1581–1590.

[85] B. J. Maron, J. A. Towbin, G. Thiene, C. Antzelevitch, D. Corrado, D. Arnett, A. J. Moss, C. E. Seidman, J. B. Young, Contemporary definitions and classification of the cardiomyopathies: an american heart association

scientific statement from the council on clinical cardiology, heart failure and transplantation committee; quality of care and outcomes research and
₁₀₀₅ functional genomics and translational biology interdisciplinary working groups; and council on epidemiology and prevention, Circulation 113 (14) (2006) 1807–1816.

[86] H. C. Strauss, J. Bigger, A. L. Saroff, E.-G. Giardina, Electrophysiologic evaluation of sinus node function in patients with sinus node dysfunction.,
₁₀₁₀ Circulation 53 (5) (1976) 763–776.

[87] A. M. Gillis, H. Puererfellner, C. W. Israel, H. Sunthorn, S. Kacet, M. Anelli-Monti, F. Tang, M. Young, G. Boriani, M. E. C. S. Investigators, Reducing unnecessary right ventricular pacing with the managed ventricular pacing mode in patients with sinus node disease and av block,
₁₀₁₅ Pacing and clinical electrophysiology 29 (7) (2006) 697–705.

[88] J. L. Cox, T. M. Sundt, Operative techniques in cardiac & thoracic surgery: A comparative atlas, Operative Techniques in Cardiac and Thoracic Surgery 1 (1) (1996) 1.

[89] F. Viola, V. Spandan, V. Meschini, J. Romero, M. Fatica, M. D. de Tul-
₁₀₂₀ lio, R. Verzicco, Fsei-gpu: Gpu accelerated simulations of the fluid-structure-electrophysiology interaction in the left heart, arXiv preprint arXiv:2103.15187.

[90] A. Loppini, A. Gizzi, C. Cherubini, E. M. Cherry, F. H. Fenton, S. Filippi, Spatiotemporal correlation uncovers characteristic lengths in cardiac
₁₀₂₅ tissue, Physical Review E 100 (2) (2019) 020201.

[91] M. Dupraz, S. Filippi, A. Gizzi, A. Quarteroni, R. Ruiz-Baier, Finite element and finite volume-element simulation of pseudo-ecgs and cardiac alternans, Mathematical Methods in the Applied Sciences 38 (6) (2015) 1046–1058.

[92] H. D. Simms Jr, D. B. Geselowitz, Computation of heart surface potentials using the surface source model, Journal of cardiovascular electrophysiology 6 (7) (1995) 522–531.

[93] D. Wang, R. M. Kirby, C. R. Johnson, Resolution strategies for the finite-element-based solution of the ecg inverse problem, IEEE Transactions on biomedical engineering 57 (2) (2009) 220–237.

[94] L. C. Lee, M. Genet, A. B. Dang, L. Ge, J. M. Guccione, M. B. Ratcliffe, Applications of computational modeling in cardiac surgery, Journal of Cardiac Surgery: Including Mechanical and Biological Support for the Heart and Lungs 29 (3) (2014) 293–302.

[95] W. Sun, C. Martin, T. Pham, Computational modeling of cardiac valve function and intervention, Annual review of biomedical engineering 16 (2014) 53–76.

[96] A. W. Lee, C. M. Costa, M. Strocchi, C. A. Rinaldi, S. A. Niederer, Computational modeling for cardiac resynchronization therapy, Journal of cardiovascular translational research 11 (2) (2018) 92–108.

[97] L. W.-T. Ng, M. Eldred, Multifidelity uncertainty quantification using non-intrusive polynomial chaos and stochastic collocation, in: 53rd AIAA/ASME/ASCE/AHS/ASC Structures, Structural Dynamics and Materials Conference, 2012, p. 1852.

[98] R. Molléro, X. Pennec, H. Delingette, A. Garny, N. Ayache, M. Sermesant, Multifidelity-cma: a multifidelity approach for efficient personalisation of 3d cardiac electromechanical models, Biomechanics and modeling in mechanobiology 17 (1) (2018) 285–300.

[99] C. M. Fleeter, G. Geraci, D. E. Schiavazzi, A. M. Kahn, A. L. Marsden, Multilevel and multifidelity uncertainty quantification for cardiovascular hemodynamics, Computer methods in applied mechanics and engineering 365 (2020) 113030.

[100] A. Barone, A. Gizzi, F. Fenton, S. Filippi, A. Veneziani, Experimental validation of a variational data assimilation procedure for estimating space-dependent cardiac conductivities, Computer Methods in Applied Mechanics and Engineering 358 (2020) 112615.

[101] A. Barone, M. G. Carlino, A. Gizzi, S. Perotto, A. Veneziani, Efficient estimation of cardiac conductivities: A proper generalized decomposition approach, Journal of Computational Physics 423 (2020) 109810.

[102] V. Meschini, M. D. de Tullio, R. Verzicco, Effects of mitral chordae tendineae on the flow in the left heart ventricle., European Physical Journal E–Soft Matter 41 (2).

[103] V. Meschini, F. Viola, R. Verzicco, Heart rate effects on the ventricular hemodynamics and mitral valve kinematics, Computers & Fluids 197 (2020) 104359.